Tunable Anisotropic Optoelectronic Properties and Scintillation Performance of Octahedrally Coordinated SiS_2 Monolayer

Vipin Kumar (विपिन कुमार)[1,*], Pushpendra Kumar[2] and Gyanendra Kumar Maurya[3]

[1]*Department of Physics, Yeungnam University, Gyeongsan-38541, Gyeongbuk-do, South Korea*

[2]*Department of Physics, Manipal University Jaipur, Jaipur-303007, Rajasthan, India*

[3]*Department of Electronics and Communication Engineering, School of Engineering, SR University Warangal, Telangana-506371, India*

Abstract: Investigation of electronic and optical properties is important for integrating the material into devices. The investigated electronic characteristics of the SiS_2 monolayer reveal that the band gap in the noble-metal-doped system increases significantly with increasing doping concentration. However, its indirect band gap features persist even after doping. A slight increase in doping concentration shifts the material's band gap. Several quantum-chemical quantities were calculated using the concepts of HOMO and LUMO energy states to gain insight into the material's kinetic stability and chemical reactivity. The investigated optical quantities depend on dopant concentration and light polarization in the visible and UV regions, suggesting the material's integration into optoelectronic devices. The polarization-dependent light absorption in the SiS_2 can be used to build on-chip polarizers and polarization-sensitive photodetectors. It is a material with a negative real dielectric constant, indicating its potential applications in super- and hyper-lenses, optical switches, and other novel optical thin-film-based components and devices. In addition to their excellent optoelectronic properties, the scintillation performance of these materials has also been evaluated. The calculated output light yield under ideal conditions is highest for the pure material, exceeding that of several reported halide-based scintillators. It is also observed that the scintillation performance is slightly reduced in the doped materials. The studied scintillation properties of SiS_2 monolayers suggest that it is a potential candidate for applications in high-energy physics, diagnostics, imaging, and security. Therefore, this work suggests that the studied materials are excellent for anisotropic optoelectronic and scintillating devices.

Keywords: Two-dimensional materials, Electronic properties, Dielectric and Optical spectra, Scintillation, Density functional theory.

1. INTRODUCTION

The characterization of two-dimensional (2D) materials has progressed rapidly in recent years, following the successful synthesis of an atomically thin single sheet of graphite [1]. Until now, many 2D materials have been experimentally and theoretically realized using various techniques [2-8]. Materials science is still advancing rapidly, both experimentally and theoretically, regarding the search for unknown 2D materials. Ab initio molecular dynamics simulations and machine learning are used to predict new 2D materials. For instance, graphene-like ionic NaX (X=F and Cl) 2D monolayers[9], group IIIA-IVA elemental 2D materials [8], chalcogen-based compounds[10], A_3BX_2-type 2D materials [11, 12], and many more [13]. Lithium metal electrodes have been recently synthesized to demonstrate long-term thermal and electrochemical stability, along with improved energy density in all-solid-state lithium batteries [14]. These low-dimensional materials also have potential applications in spintronic device technology [15]. Several 2D materials have been explored experimentally and theoretically for potential applications in sensing technology [16], catalysts [17], and optoelectronics [18, 19].

The chalcogenide-based group-IVA compounds have attracted significant research interest due to their exotic physical and chemical properties [20-25]. 1T-SnS_2 nanosheets were recently synthesized using mechanical exfoliation to exhibit a thickness-dependent out-of-plane piezoelectric response [26]. GeS_2 monolayers were also investigated using first-principles methods for their adsorption behavior toward various toxic gases [27]. Inspired by these studies, group IVA-VIA 2D compounds have garnered significant research interest due to their large bandgap and intrinsic semiconducting properties. SiS_2 is also crystallized in 2D with various structures and belongs to a family of IVA-VIA 2D compounds [28, 29]. Group-VIA compounds exhibit layered solid structures between the ambient and high pressure. Ab initio molecular dynamics (AIMD) simulations combined with first-principles calculations predicted three distinct phases ($R\bar{3}m$, $P\bar{3}m1$, $P6_3mc$) of SiS_2 2D layers, in which the Si atom is octahedrally coordinated to the S atom. It has been reported that these structures are more stable than those with tetragonal coordination. $P\bar{3}m1$ is the most stable phase of the SiS_2 2D monolayer up to 100 GPa with the lowest enthalpy [30]. All three phases of SiS_2 show a continuous decrease in

*Address correspondence to this author at the Department of Electronics and Communication Engineering, School of Engineering, SR University Warangal, Telangana-506371, India; E-mail: kumar.vipin118@gmail.com

Received on 05-09-2025 Accepted on 11-10-2025 Published on 13-10-2025

E-ISSN: 3110-9772/25

the indirect band gap with increasing pressure. This system metallizes at an applied pressure of around 30 GPa. The $P\bar{3}m1$ phase of the SiS_2 monolayer shows a bandgap of around 2.0 eV at 10 GPa, and the metallization occurs at 40 GPa. This material transitions from an indirect-bandgap semiconductor to a poor metal at 40 GPa with overlapping bands between the Γ and K points. It remains a poor metal even at 100 GP, showing a low density of states around the Fermi energy [30]. The $P\bar{3}m1$ phase of SiS_2 monolayer was detected in the XRD pattern on compressing it above 7.4 Gpa [31], consistent with the Raman active vibrational modes predicted using group theory.

SiS_2 monolayers fit into the landscape of functional thin films as a next-generation 2D material with a powerful suite of customizable properties. Its semiconducting nature, tunable bandgap, unique optical profile, and auxetic properties position it as a versatile candidate for applications in optoelectronics, energy storage, and flexible nano-mechanics [32, 33]. It expands the current materials toolkit beyond conventional films like SiO_2 and broadens the possibilities for designing future technologies. It can also be combined with other 2D materials to form heterostructures. For example, a SiS_2/WSe_2 heterostructure has shown type-II band alignment, which promotes the separation of electron-hole pairs [34]. This is a desirable property for improving the efficiency of photoelectric devices. It exhibits a tunable bandgap that can be modified by applying external strain [35]. This feature is critical for tailoring the material for specific applications, such as adjusting the absorption wavelength in solar cells. However, the SiS_2/BSe heterojunction is a promising candidate for photocatalytic water splitting [36].

A scintillator is a material that converts incident ionizing radiation into low-energy photons, a main feature of the scintillation detector. Scintillators based on inorganic materials have been widely explored for applications [37, 38]. These studies have identified materials that exhibit several common properties, such as high light yield, fast decay time, and high density [39, 40]. These properties are important for achieving high efficiency and high resolution. However, these specifications for scintillating material are not obtained in all studied materials. Some are either expensive, hygroscopic, or take an extended synthesis time. A few recent studies reported halide-based materials for scintillation purposes. For example, Tl-based halide materials exhibit promising scintillation properties for X-ray and γ-ray detection [40-42]. Specifically, $TlMgCl_3$ has an advantage over other scintillating materials: it is non-hygroscopic and exhibits self-activated scintillation, eliminating the need for doping [43, 44]. Hence, it enables low-cost, homogeneous, and large-scale material growth. A few studies reported the characterization and scintillating properties of halide compounds. A few common optical properties of a high-performance scintillating material that can maximize its detection efficiency are a low reflection coefficient, a high index of refraction, and a low absorption coefficient [37, 38].

Unprecedented success in synthesizing the stable phase of the 2D SiS_2 monolayer has led to enormous research interest in its properties for various applications. The electronic properties of the 2D SiS_2 monolayer have already been explored [28, 29, 33, 34]. High light absorption in SiX_2 (X=S, Se, and Te) monolayers in the ultraviolet region indicates their potential for nanoelectronics and optical devices [45]. Under applied uniaxial strain, it is transparent to both infrared and visible light. Its optical properties change significantly along the zigzag and armchair directions in the presence of an uniaxial strain [35]. Doping with pnictogen atoms can tune the magnetic and electronic properties of SiS_2 monolayers [46]. The doping method has been applied to several 2D materials to modify their electronic and optical response [47-49]. However, the noble-metal-doped SiS_2 monolayer has not been reported to the best of our knowledge. Therefore, this study aims to investigate the effect of noble metal (Pt) doping on the electronic, optical, and scintillation properties of the SiS_2 monolayer. The impact of varying dopant concentrations is also investigated. The electronic and optical response of the metal-doped SiS_2 monolayer changes significantly, suggesting its potential for optoelectronic device applications and making it a good candidate for scintillation detectors.

2. COMPUTATIONAL AND CALCULATION DETAILS

We use the OpenMX simulation package to perform all density functional theory (DFT) calculations using the norm-conserving pseudopotentials within the generalized gradient approximations (GGA). The exchange-correlation potential is treated with the Perdew-Burke-Ernzerhof (PBE) functionals. Cell vectors and atomic coordinates were simultaneously relaxed using the variable-cell optimization scheme. It uses the combined rational functions (RF) and the direct inversion iterative subspace (DIIS) method. The approximate Hessian is used for the BFGS update. The variable-cell optimization runs iteratively until the force on each atom is equal to or less than $3x10^{-4}$ Hartree/Bohr. The kinetic energy cutoff of 240 Ry is used for the internal coordinates and cell vector relaxation. The energy convergence criterion for the self-consistent iterations was set to 10^{-6} Hartree. The

Kohn-Sham wave functions were expanded using the optimized pseudoatomic basis sets. The basis sets used for Si, S, and Pt are tabulated in Table **1**. For example, Si7.0-s2p2d1 means that two, two, and one optimized basis radial functions are used for s, p, and d orbitals, respectively, for Si and S atoms, where 7.0 indicates the used cutoff radius. Similarly, the optimized basis radial functions used for S and Pt atoms can be explained. The Fermi-Dirac function accounts for the number of electrons at 700K during the SCF calculations. The self-consistent iterations were performed using a 9x9x1 k-point mesh. The doping concentration in a 3x3x1 SiS_2 supercell was varied by increasing the number of dopant atoms. In this study, Pt-atom, a member of noble metals, was used as a dopant. We modelled a 3x3x1 SiS_2 supercell doped with one, two, and three Pt-atoms, corresponding to a doping (percentage) concentration of 3.70%, 7.41%, and 11.11%, respectively. The electronic calculations were performed using a 21x21x1 k-point mesh. The inter-layer interactions were avoided using a vacuum space greater than 15 Å along the c-axis of the 2D SiS_2 monolayer. However, the dielectric and optical calculations were performed with a 21x21x1 k-point mesh. The OpenMX simulation package calculates dielectric functions and other optical quantities using the Kubo-Greenwood formula for conductivity and dielectric tensors, which involves calculating matrix elements [50, 51] between the filled and empty electronic states.

Table 1: List of used Basis Sets in the DFT Calculations

Si7.0-s2p2d1	S7.0-s2p2d1f1	Pt7.0-s3p2d2

3. RESULTS AND DISCUSSIONS

3.1. Structural Optimization and Electronic Properties

Group IVA-VIA monolayer compounds have attracted significant research attention due to their unique structural and electronic properties. Free-standing SiS_2 single layer is also a member of the group IVA-VIA monolayer compounds. It belongs to the $p\bar{3}m1$ space group. We consider the 1T phase of the SiS_2 single layer. Its unit cell has three atoms: one Si atom and two S atoms. In the SiS_2 monolayer, the Si and S atoms are arranged in an S-Si-S layer pattern, *i.e*., two S-atomic layers on either side of a Si-layer in the middle. In other words, it is a quasi-2D planar material with a hexagonal symmetry. This hexagonal symmetry can be seen from the Si-atoms bonded to the six nearest neighboring S-atoms (an octahedral coordination between SI and S-atoms). In this hexagonal structure with $p\bar{3}m1$ space group, the Si and S-atoms are positioned at 1a and 2d Wyckoff positions. The optimized crystal structure of the SiS_2 monolayer (front and side views) in a 3x3x1 supercell approach is shown in Figure **1**(**a**) and **1**(**b**). The Si-S bond length and S-S distance along the c-axis (*i.e*., the buckling height) are denoted by $d_{Si\text{-}S}$ and h, respectively, see Figure **1**(**b**). After fully relaxing the geometrical structure in the variable cell optimization technique, discussed earlier in section 2, the following crystal structure parameters were obtained: (i) lattice constant a = b = 3.31 Å, (ii) Si-S bond length $d_{Si\text{-}S}$ = 2.33 Å, (iii) buckling height h = 2.64 Å, respectively. These are indicated in Figures **1**(**a**) and (**b**), respectively. These calculated optimized parameters are also listed in Table **2** and compared with previously reported works. The lattice parameters obtained for the SiS_2 monolayer are close to the reported values, indicating that the structure is well converged. These parameters are suitable for investigating the electronic properties.

However, we aim to exploit the electronic and optical properties of the noble metal-doped SiS_2 monolayer. The Pt-atom from the family of noble metals is chosen as a dopant in the SiS_2 monolayer system. Substitutional doping is popular among the computational and simulation scientific community. In substitutional doping, one or more atoms in the host material are replaced by foreign atoms, called dopants. For example, we have substituted one Si-atom (say the thirteenth Si-atom) with a single Pt-atom as displayed in Figure **1**(**c**) (front view) and **1**(**d**) (side view), respectively. Again, the structural optimization was performed for the single Pt-atom-doped SiS_2 monolayer using the variable-cell optimization method. The single Pt-atom doping in a 3x3x1 supercell of the

Table 2: Comparison between the Obtained and Reported Lattice Parameters of the SiS_2 Monolayer

Structure	Lattice parameters					
	Present work			Reported works		
	a (Å)	h (Å)	$d_{Si\text{-}S}$ (Å)	a (Å)	h (Å)	$d_{Si\text{-}S}$ (Å)
1T-SiS_2	3.31	2.64	2.33	3.28[45], 3.21[35], 3.32[32], 3.29[36]	2.68[45], 2.64[46], 2.66[32]	2.32[36,46], 2.33[32]

SiS_2 monolayer corresponds to the 3.70% doping concentration of the dopant atom. We named this system SiS_2-Pt@3.70%, and the undoped system is denoted as SiS_2-Pt@0%. The optimized structure SiS_2-Pt@3.70% is shown in Figure **1**(**c**) and **1**(**d**), where the optimized lattice parameters were also indicated. Doping leads to local structural modifications, including changes in bond lengths and lattice parameters. The doping slightly increases the lattice constant from 3.31 Å to 3.36 Å, corresponding to a 1.51% increase relative to the SiS_2-Pt@0% sample. All the first nearest neighbors (S-atoms) of the dopant atom (Pt-atom) significantly change their position, leading to a modification in the Pt-S bond length. The second and third-nearest neighbors also rearrange themselves after doping. This atomic rearrangement after noble metal Pt-doping leads to modification of the Si-S bond length surrounding the dopant atom. The Pt-S and Si-S bond lengths after structural optimization are indicated in Figure **1**(**c**). The doping locally distorts the crystal structure; however, the atomic arrangement far from the dopant site remains almost unchanged. The estimated nearest Pt-S bond length is 2.40 Å, comparable to the pure PtS_2 monolayer [52]. However, the calculated nearest and next nearest Si-S bond lengths with respect to the dopant atom are 2.32 Å and 2.35 Å, respectively, Figure **1**(**c**). The Si-S bond length, further away from the dopant site, is almost the same as in an undoped SiS_2 system. It justifies the claim that the doping distorts the host structure locally. It is noticed that the lattice constant increases with increasing doping concentration. The lattice constants of two and three Pt-atom doped SiS_2 (*e.g.*, SiS_2-Pt@7.41% and SiS_2-Pt@11.11%) are estimated to be 3.37 Å and 3.40 Å, respectively. The optimized structures of SiS_2-Pt@7.41% and SiS_2-Pt@11.11%, along with their lattice constants, are displayed in Figure **S1**(**a**) and **S1**(**b**) of the supplementary information (SI), respectively. This gradual increase in the lattice constant is obvious because the increasing doping concentration led to the gradual transformation of SiS_2 to PtS_2. The reported lattice constant of the PtS_2 monolayer is 3.59 Å [52]. Moreover, the SiS_2 monolayer is dynamically, thermally, and mechanically stable [46]. Structural stability is another important concern in the experimental synthesis of a material. Therefore, before discussing its properties, we briefly shed light on the thermodynamic stability of the doped and undoped SiS_2 monolayers. It is calculated for each case using the concept of the cohesive energy, defined as follows,

$$E_C = \frac{\sum_i n_i E_i - E_T}{\sum_i n_i} \quad (1)$$

Here, E_T stands for the total energy of the doped/undoped systems. E_i represents the constituent atom's (Si, S, and Pt) energy in a free state, and n_i is the corresponding total number of atoms. For example, in SiS_2-Pt@0%, there are nine Si-atoms ($n_{Si} = 9$) and eighteen S-atoms ($n_S = 18$). Similarly, for SiS_2-Pt@3.70%, there are eight Si-atoms ($n_{Si} = 8$), eighteen S-atoms ($n_S = 18$), and a

Single Pt atom ($n_{Pt} = 1$), and so on. According to the definition of the cohesive energy in Eq. (1), the more positive energy corresponds to the strong structural-chemical stability. In other words, cohesive energy measures the strength of bonding between the

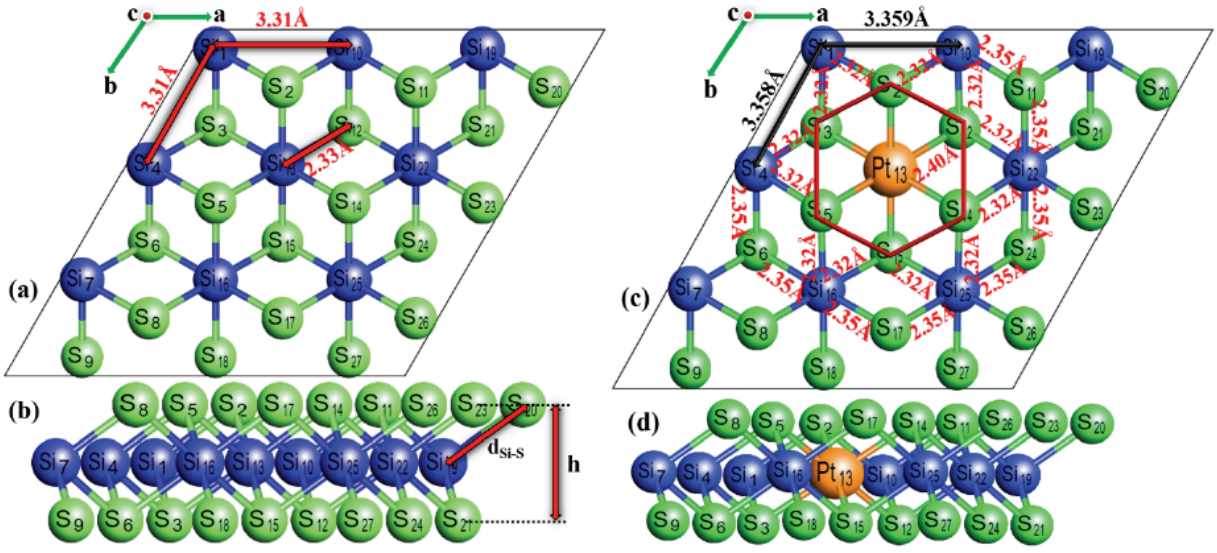

Figure 1: Optimized crystal structure in the supercell approach. Front (**a**) and side (**b**) views of the pure SiS_2 monolayer, respectively. (**c**) and (**d**) are the front and side views of the 3.70% Pt-doped SiS_2 monolayer, respectively. The 3.70% doping corresponds to the single Pt-atom doping in the 3x3x1 supercell of the SiS_2 single layer. The optimized lattice parameters and various d_{Si-S} bond lengths are mentioned in their respective diagrams, where h denotes the buckling height and d_{Si-S} is the Si-S bond length.

constituent elements/atoms in a material or compound. In this work, the calculated cohesive energy of the pure SiS_2 monolayer supercell (SiS_2-Pt@0%) is nearly 11.65 eV. However, the cohesive energy of the doped SiS_2 monolayer is slightly enhanced with an increase in the Pt-doping concentration. The cohesive energy of the Pt-doped SiS2 monolayer is in the following order: SiS_2-Pt@0% (11.65 eV) < SiS_2-Pt@3.70% (13.86 eV) < SiS_2-Pt@7.41% (15.98 eV) < SiS_2-Pt@11.11% (18.01 eV), respectively. The increasing cohesive energy of the SiS_2 monolayer with increasing Pt-doping concentration shows strong thermodynamic stability of the respective structure. Hence, the highly Pt-doped SiS_2 monolayer possesses strong thermodynamic stability. A highly thermodynamically stable structure indicates that the constituent atoms are more strongly bonded to each other. Hence, the structural configuration is more energetically favorable than atoms in their free state. The reported values of the cohesive energy of a pure SiS_2 monolayer unit cell are 4.23 eV/atom [32] and 4.73 eV/atom [45]. Another way to determine the dynamical stability of a crystal configuration is the phonon dispersion along the high-symmetry BZ. The absence of imaginary frequencies in the phonon spectrum is a characteristic feature of a dynamically stable structure [45]. It is shown that the phonon spectrum exhibits nine vibrational modes around the Γ −point, including three low-frequency acoustic vibrations and six high-frequency optical vibrational modes (see Figure **2** of ref [45]). Ab initio molecular dynamics (AIMD) simulation is another way to examine structural thermal stability, Figure **2**(**c**) in ref. [46]. The temperature was observed to fluctuate slightly around 300K, suggesting that the SiS_2 monolayer is thermally stable. Moreover, these temperature fluctuations do not rupture bonds between the constituent atoms. These results are sufficient to demonstrate that the materials under investigation possess strong structural stability and can be used to investigate their physical and chemical properties.

A few quantum chemical parameters have been calculated to gain further insight into kinetic stability and chemical reactivity. These quantum-chemical parameters are estimated using the concepts of the highest occupied molecular orbital (HOMO) and the lowest unoccupied molecular orbital (LUMO), which together form the frontier molecular orbitals (FMO). These molecular orbitals (MOs) are important in understanding the electronic structure, kinetic stability, chemical reactivity, and optoelectronic properties. The HOMO-LUMO isosurfaces are displayed in Figure **S2** of the **SI**. Determining these energy levels is crucial for integrating different materials into efficient devices, such as transistors, solar cells, and light-emitting diodes (LEDs). The energy difference between the HOMO and LUMO energy levels is known as the HOMO-LUMO energy gap (ΔE_g). Generally, it is the lowest possible energy for electronic excitations in a compound. A large HOMO-LUMO gap indicates that the electron excitation requires a high amount of energy from a lower to a higher energy level. It also corresponds to the minimum amount of energy required for an electronic transition to occur in a material and for it to conduct electricity. On one hand, the HOMO energies determine the electron-donating (or losing) ability. On the other hand, the LUMO energies are responsible for the electron-accepting (receiving or gaining) ability. In other words, the energies corresponding to HOMO and LUMO can be termed the ionization potential (IP) and electron affinity (EA), respectively [53]. The low-energy HOMO levels indicate that the respective compound has a greater tendency to lose electrons. The ΔE_g is an important parameter in understanding the material's kinetic stability and chemical reactivity. A larger HOMO-LUMO gap indicates that the material is more chemically hard and less chemically reactive. The high chemical hardness indicates stability.

The HOMO-LUMO energy gap concept is applied to understand the chemical kinetics and reactivity of pure and doped SiS_2 monolayers. Various quantum-chemical parameters are listed in Table **3** and were determined from the HOMO (E_{HOMO} = IP) and LUMO (E_{LUMO} = EA) energy levels. The quantum chemical quantities are determined from the following formulae[54–56],

Absolute electronegativity, $\chi = -\frac{E_{HOMO}+E_{LUMO}}{2} = -\mu$ (2)

Chemical hardness, $\eta = \frac{E_{LUMO}-E_{HOMO}}{2} = \frac{\Delta E_g}{2}$ (3)

Chemical softness, $\sigma = \frac{1}{2\,\eta} = \frac{1}{\Delta E_g}$ (4)

Electrophilicity index, $\omega = \frac{\chi^2}{2\,\eta} = \frac{\chi^2}{\Delta E_g} = S \times \chi^2$ (5)

The HOMO and LUMO energy levels are schematically drawn in Figure **2**. A decreasing trend of ΔE_g with increased Pt-doping concentration was predicted. The ΔE_g is in the following order: SiS_2-Pt@0%>SiS_2-Pt@3.70%>SiS_2-Pt@7.41%>SiS_2-Pt@11.11%. The energies corresponding to HOMO and LUMO are crucial in determining the mentioned quantum-chemical quantities. In the context of molecular orbital theory, these energy levels are also used to determine the approximate value of the ionization potential (IP) and electron affinity (EA) as follows: IP = - E_{HOMO} and EA = - E_{LUMO}. Hence, the quantum-chemical parameters discussed above can also be represented in terms of the IP and EA. However, the calculated values of these parameters are listed in Table **3** using the formulae mentioned

Table 3: Various Quantum Chemical Parameters of Pure and Doped SiS_2 Monolayers

system	Quantum Chemical Parameters in Units of eV.						
	E_{HOMO}	E_{LUMO}	ΔE_g	$\chi(=-\mu)$	η	σ	ω
SiS_2-Pt@0%	-6.52	-4.04	2.48	5.28	1.24	0.40	11.24
SiS_2-Pt@3.70%	-6.33	-4.06	2.27	5.20	1.14	0.44	12.28
SiS_2-Pt@7.41%	-6.23	-4.11	2.12	5.17	1.06	0.47	12.61
SiS_2-Pt@11.11%	-6.28	-4.28	2.00	5.28	1.00	0.50	13.94

above in terms of the HOMO and LUMO energies and ΔE_g. The lowest LUMO energy level signifies the electron acceptor level, whereas, the highest energy corresponding to the HOMO level indicates the strong electron-donating capability. In the doped material, these are expected to shift relative to the undoped case (see Figure **2**).

The absolute electronegativity (χ) indicates how strongly a system attracts electrons. It can be determined from the molecular orbital (MO) energies using Eq. (2). The larger χ corresponds to the strong electron-attracting ability of a particular material or compound, indicating a large amount of charge transfer. For example, the value of χ is maximum for the undoped SiS_2 monolayer, and decreases slightly with a small doping percentage. However, a large doping amount again increases its value. This means the SiS_2 monolayer has a strong ability to attract an electron. The χ is also related to the electronic chemical potential (μ) by the relation $\chi = -\mu$. The μ indicates the charge transfer and, hence, the chemical reactivity of compounds. In other words, materials with high χ and μ are more reactive because such materials have a strong ability to attract electronic charges. Therefore, undoped SiS_2 exhibits strong charge-attracting capability and is a strongly chemically reactive material. However, its electron attraction capability and chemical reactivity can be further improved in the highly Pt-doped system due to the large χ and μ.

The chemical hardness (η) measures the material's ability to resist or permit the charge transfer. It can be determined from Eq. (3), expressed in terms of the HOMO/LUMO levels energy and ΔE_g. According to Eq. (3), it is just half of the HOMO-LUMO bandgap. Its high value indicates that the material strongly resists charge transfer, showing that the respective material is chemically hard and vice versa. It suggests that increasing the Pt-doping concentration reduces the chemical hardness of SiS_2 and shows less resistance to charge transfer. Simultaneously, its stability decreases slightly with an increased Pt-doping concentration. Moreover, its low value also indicates that the material is strongly chemically reactive. Hence, the material with a high value of χ or μ and a low value of η exhibits strong chemical reactivity. The highly Pt-doped SiS_2 is a less hard material; it shows strong chemical reactivity and slightly reduced stability. Collectively, a material with a large HOMO-LUMO gap shows its high kinetic stability and hardness, and vice versa. The softness index (σ), Eq. (4), determines the material's capacity to receive electrons. A high σ value indicates that the material is soft. The increasing trend in the softness index shows that SiS_2 softness increases with increasing Pt-doping concentration. It further supports the increased chemical reactivity of the highly Pt-doped SiS_2 monolayer. The electrophilicity index (ω), Eq. (5), determines the material's electron-accepting ability and resistance to electron

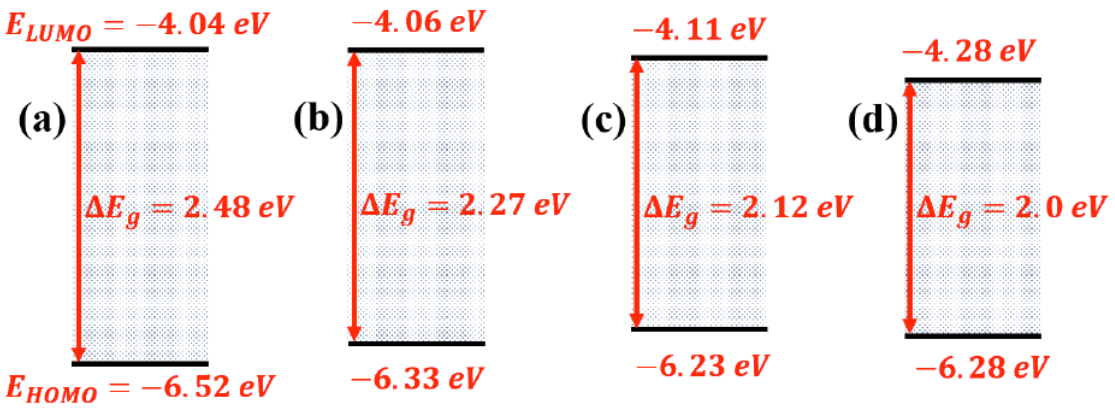

Figure 2: Highest occupied molecular orbital (HOMO) and lowest unoccupied molecular orbital (LUMO) energy levels in pure and doped SiS_2 monolayers. (**a**) SiS_2-Pt@0%, (**b**) SiS_2-Pt@3.70%, (**c**) SiS_2-Pt@7.41%, and (**d**) SiS_2-Pt@11.11%, respectively.

exchange with surroundings. A high value of ω supports large electron transfer between the acceptor and donor species. It means that a material with a high ω (*e.g.*, high μ and low η) is highly electrophilic, favors strong electronic transfer between the donor and the acceptor, and offers less resistance to charge transfer. In the present case, for example, the electrophilicity index (ω) increases remarkably with increasing Pt-doping concentration. It is maximum (=13.94) for 11.11% Pt-doped SiS_2 monolayer, indicating that Pt@7.41%>SiS_2-Pt@11.11% is a strong electrophile. Hence, it tends to accept additional electrons from its surroundings and is less resistant to electron transfer. These quantum-chemical parameters have been discussed in ref [57] for a few organic molecules.

Next, we investigated the electronic properties of pure and Pt-doped SiS_2 monolayers using the optimized structural details. These electronic properties were calculated along the Γ-M-K-Γ path of the 2D hexagonal Brillouin zone (BZ). The electronic structure and DOS of pure SiS_2 monolayer (*e.g.*, SiS_2-Pt@0%) are elucidated in Figure **3**. In the case of a pure SiS_2 monolayer, the valence band maximum (VBM) is located between the Γ- and M-points, Figure **3**(**a**). However, the conduction band minimum (CBM) lies at the M-point. The indirect band gap obtained in the pure SiS_2 monolayer is nearly 1.42 Å, comparable to the reported values in Table **4**. However, the obtained bandgap values using the PBE are smaller than those using the HSE exchange-correlation potential. In the HSE exchange-correlation potential within the GGA approximation, the reported bandgap values of the pure SiS_2 monolayer are 2.22 eV [45], 2.34 eV [32], and 2.45 eV [34]. The underestimation of the bandgap in the PBE functional is due to the self-interaction error, which can be corrected by using a hybrid functional such as HSE. The total DOS in Figure **3**(**b**) corroborates the band structure of SiS_2-Pt@0% in Figure **3**(**a**).

The electronic properties of the pure SiS_2 monolayer were reported in several studies, as discussed above. The electronic properties of the pure

Table 4: Comparison of the Calculated and Reported Bandgap (E_g, eV) Values of Pure SiS_2 Monolayer. CHANGES in Bandgap Values and the Positions of the VBM and CBM with Increasing Doping Concentration are also Noted

System	SiS_2-Pt@0%	SiS_2-Pt@3.70%	SiS_2-Pt@7.410%	SiS_2-Pt@11.11%
This work (bandgap)	1.42	1.79	1.80	1.82
Others[ref] (bandgap)	1.33[45], 1.36[32], 1.39[34]	-	-	-
CBM (eV) VBM (eV)	0.68 -0.74	0.87 -0.92	0.89 -0.91	0.88 -0.94

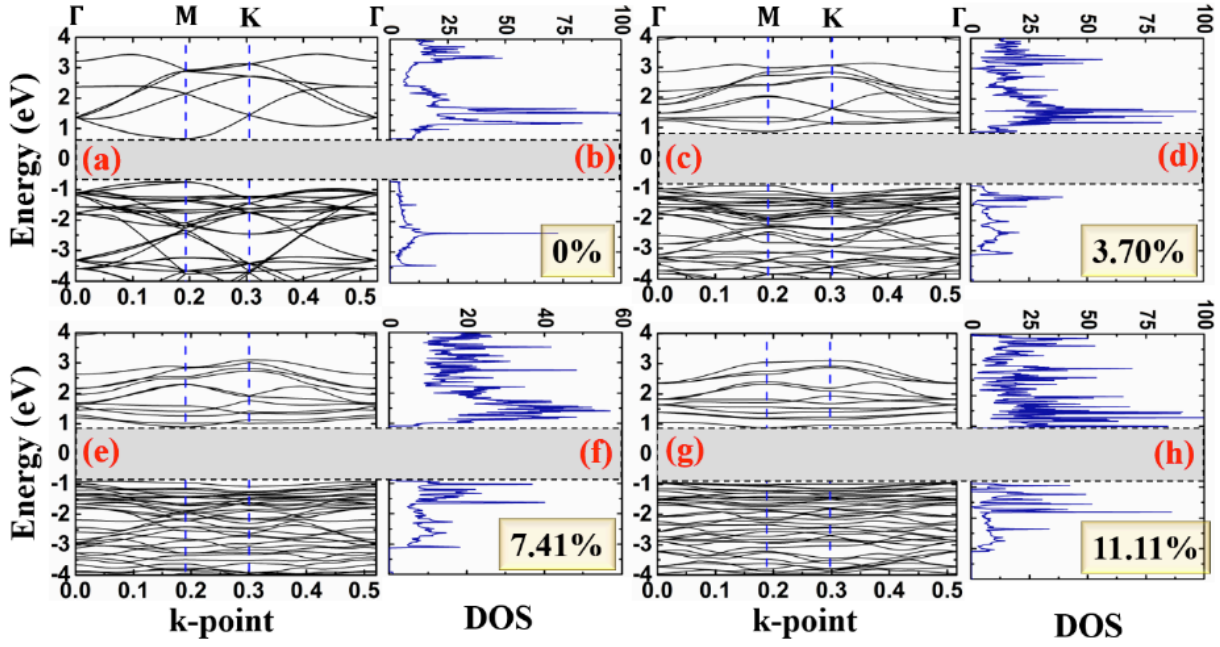

Figure 3: Electronic band structures and total density of states of the pure and doped SiS_2 monolayers. (**a**), (**c**), (**e**), and (**g**) are the band structures of 0%, 3.70%, 7.41%, and 11.11% Pt-doped SiS_2 monolayer, whereas (**b**), (**d**), (**f**), and (**h**) are their corresponding total density of states, respectively.

SiS_2 monolayer can be modified in several ways. The doping methods to change its electronic properties are one of them. A Pt atom from the family of noble metals is chosen for the substitutional doping in the SiS_2 monolayer. A Pt-atom is inserted by replacing a single Si-atom in the host SiS_2 monolayer; *e.g.*, we doped a 3x3x1 supercell of the pure SiS_2 monolayer, containing a total 27 number of atoms, with a single Pt-atom. It corresponds to a 3.70% Pt-doping. The SiS_2 monolayer doped with a single Pt atom is denoted as SiS_2-Pt@3.70%. Therefore, in this work, efforts have been made to investigate the effect of Pt-doping on the structural and electronic properties. This doping leads to the locally distorted crystal structure discussed earlier. The effect of a single Pt-atom doping on the electronic band structure and DOS is illustrated in Figures **3**(**c**) and **3**(**d**), respectively. It is clear from these figures that the band gap increases significantly after substitutional Pt-atom doping at one of the Si sites (*e.g.*, the thirteenth Si atom, see Figure **1**). The doping shifts the CBM and VBM towards the up and down sides, respectively, with respect to the zero-energy level. It increases the separation between the VBM and CBM, thereby increasing the bandgap of the SiS_2 monolayer material. However, its indirect bandgap is preserved. In other words, doping does not change the indirect bandgap characteristic of the SiS_2 monolayer, even after doping. Moreover, additional electronic states in the VB and CB are evident. The doping-induced effect on the band structure is justified by the total DOS, shown in Figure **3**(**d**). The absence of DOS between the VBM and CBM justifies the corresponding increased bandgap in the SiS_2-Pt@3.70% monolayer.

We have also studied the effect of varying Pt doping on the band structure and DOS, which is still an open question. For this purpose, we increased the doping concentration by adding dopant atoms to a 3x3x1 SiS_2 supercell. The electronic band structures of two and three Pt-atom-doped SiS_2 monolayers are shown in Figures **3**(**e**) and **3**(**g**), respectively. These two systems correspond to 7.41% and 11.11% doping of Pt atoms and are denoted as SiS_2-Pt@7.41% and SiS_2-Pt@11.11%, respectively. Doping also leads to more electronic states appearing in the electronic band structure. It is observed that the bandgap changes are insignificant with the Pt-atom doping concentration. It can be further justified from the total DOS shown in Figures **3**(**f**) and **3**(**h**), respectively. The bandgap variation pattern is shown in Table **4**, along with the position of the VBM and the CBM. Moreover, it has been observed that increasing the Pt-atom doping concentration does not significantly change the electronic properties. Therefore, we restrict ourselves to discussing the varying doping concentration (*e.g.*, SiS_2-Pt@3.70%) and compare the results with those of the pure material (*e.g.*, SiS_2-Pt@0%).

Insights into the obtained electronic properties can be drawn from the projected DOS shown in Figures **4**(**a**-**c**) for SiS_2-Pt@0% and Figures **4**(**d**-**f**) for

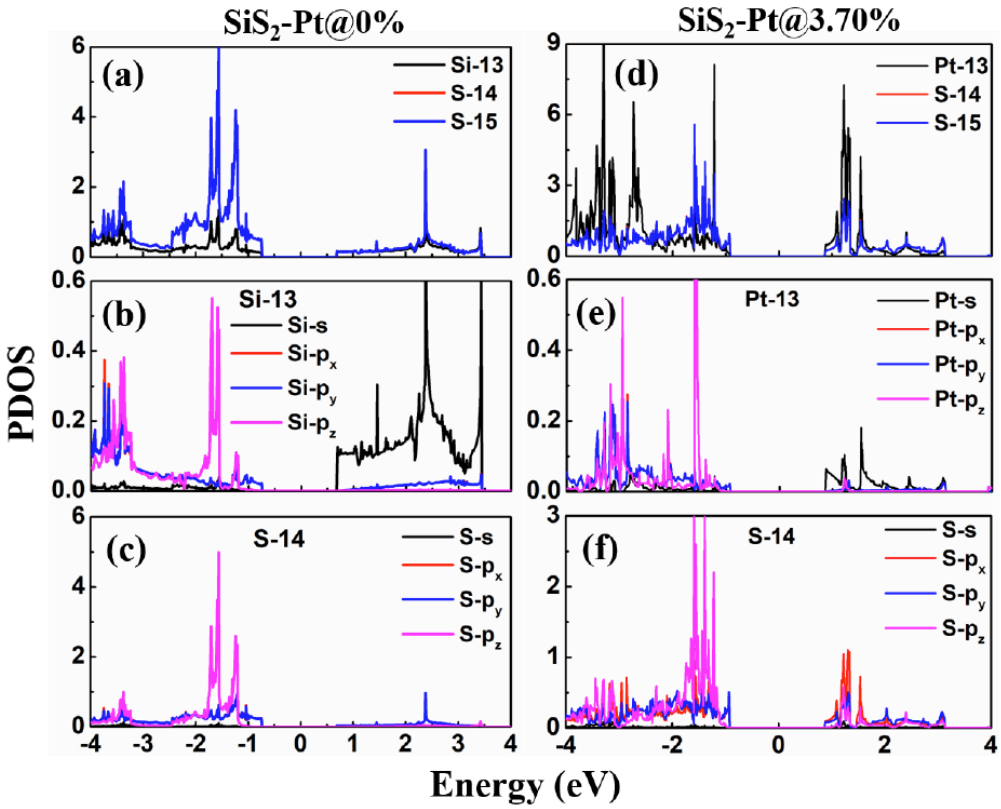

Figure 4: Projected density of states of (**a**-**c**) SiS_2-Pt@0% and (**d**-**f**) SiS_2-Pt@3.70%.

SiS_2-Pt@3.70%, respectively. For the pure and 3.70% doped cases, we have calculated the atomic- and orbital-projected DOS. Both are calculated for atoms at the dopant site (*e.g.*, the thirteenth atom, see Figure **1**) and nearest neighbors. These are either the Si and S-atoms in the host or the Pt-S atoms in the doped system. Figures **4**(**a**-**c**) show the DOS of the constituent atoms of the host material (*e.g.*, the thirteenth Si atom and the nearest bonded S atom, say atoms fourteen and fifteen). Whenever the specific atom number is mentioned, readers should refer to Figure **1** for specifications. It is evident from Figure **4**(**a**) that the atomic projected DOS of both of the octahedrally connected S-atoms (for example, atoms S_{14} and S_{15}) to the Si_{13}-atom in the pure SiS_2 monolayer overlap on one another, signifying that DOS of both of these atoms (blue color, for S_{15}, hiding the red color for S_{14}) are contributing equally to the total DOS. The Si and S atoms contribute significantly to the TDOS of the pure SiS_2 monolayer. The orbital-projected DOS shows that S-p_z contributes more to the VB than the equal contributions from S-p_x and S-p_y, see Figure **3**(**c**). However, the S-p_x and S-p_y orbitals contribute to the VBM, and the Si-s orbital predominantly contributes to the CBM, see Figure **4**(**b**), with a comparatively small contribution from the S-p_x and S-p_y orbitals. The S-s orbital has a negligible contribution to the total DOS, see Figure **4**(**c**), of the pure SiS_2 monolayer. In other words, from the above discussion, it can be stated that the electronic states in the upper part of the VB are predominantly due to the S-p orbitals. In contrast, the energy states in the CB mainly originate from the Si-s orbital. Moreover, electronic hybridization can be noticed in both the VB and the CB. These findings agree with other reported works [35, 46].

The orbital projected DOS of a single Pt atom doped SiS_2 monolayer (*e.g.*, SiS_2-Pt@3.70%) is displayed in Figures **4**(**d**-**f**). It is seen that the Pt-atom has a significant contribution in modifying the electronic properties of the SiS_2 monolayer. It dominantly contributes to the total DOS in both the VB and CB. The S-p_x and S-p_y orbitals predominantly contribute to the VBM, while the Pt-s and Pt-p orbitals have a negligible contribution. The S-p_z and Pt-p_z orbitals contribute to the deep-lying VB and CB electronic energy states. Similarly, Pt-s, S-p_x, and S-p_y orbitals form the CBM. Most importantly, electronic hybridization between different Pt and S orbitals is evident in both the VB and the CB. It indicates an electron-sharing feature, showing a strong covalent bonding between the Pt- and S-atoms. Due to the electronegativity difference between the Pt and S atoms, a small amount of charge transfer occurs between them. It shows a slight ionic character of the Pt-S bond. Hence, Pt-S bonds in the SiS_2-Pt@3.70% exhibit the coexistence of covalent and ionic bond features. The electron sharing and hybridization between the Pt- and S-orbitals can be confirmed from the total electron densities of each system, Figure **S3** of the SI. Figure **S3**(**a**) shows that the total electron density enriched sites are mainly at S-atoms, indicating that the Si-S bonds are predominantly ionic. The same observations have been made by calculating the electron localization function (ELF). It is observed that the electrons are highly localized around the S atomic sites, indicating the ionic character of Si-S bonds in the SiS_2 monolayer [46]. The ionic character of Pt-S bonds in SiS_2-Pt@3.70% is clear from Figure **S3**(**b**). Due to the electronegativity difference, the electron density on Pt- and S-atoms is slightly stretched along the Pt-S bond length direction. Similar features can also be seen for SiS_2-Pt@7.41%, Figure **S3**(**c**), and SiS_2-Pt@11.11%, Figure **S3**(**d**). The Mulliken charge scheme is used to visualize[58] the net charge on each constituent atom of the pure and doped SiS_2 monolayer, illustrated in Figures **S4** and **S5**. It is seen that the Si-atom is an electron loser, whereas S-atoms behave like electron acceptors. This analysis indicates that the Si-atom can transfer 0.475 electronic charges to each S-atom bonded to it, Figure **S4**(**a**). A similar phenomenon is also seen in the Pt-doped SiS_2 systems, supporting the coexistence of covalent and ionic bond features in all the doped SiS_2 monolayers, Figures **S4** and S5 of the SI. The difference electron density is measured from the individual atomic densities in each system, as depicted in Figures **S6**. Figure **S6**(**a**) shows that the electron-rich density regions are mostly located around the Si atom, showing its electronic donor features. A small electron density localization between the Si-S bond further supports the covalent bonding. The difference electron density is redistributed after Pt-atom doping, illustrated in Figures **S6**(**b**-**d**). A significant depletion of the difference electron density was noticed on the Pt-atom and the region along the Pt-S bond. Simultaneously, small difference electron density accumulation and depletion regions were observed around S- and Pt-atoms, respectively. It again asserts the coexistence of covalent and ionic bonding in the doped SiS_2 systems. The difference electron density exhibits similar features as the doping concentration varies, as shown in Figures **S6**(**c**) and **S6**(**d**). In short, the electronic band structure and DOS calculations show that the pure and Pt-doped SiS_2 monolayers are an indirect bandgap semiconducting material. However, the bandgap in the Pt-doped SiS_2 monolayer is significantly increased. Moreover, these materials exhibit both partial covalent and ionic bonding characteristics. These findings suggest that the bandgap of the SiS_2 monolayer can be tuned by

suitable doping, making it useful for electronic and optoelectronic devices.

3.2. Dielectric Response and Optical Properties

The dielectric response is a material-dependent property. It is determined by estimating the dielectric function or dielectric permittivity. The dielectric function is a quantity that describes how a material responds to an applied electric field, relating the field strength to the induced polarization. It is a frequency-dependent quantity that characterizes the dielectric dispersion. There is a time lag between the change in the polarization direction and the applied field. Hence, the dielectric function (permittivity) is a complex function of the frequency of the applied field. This frequency-dependent complex function plays a vital role in determining the optical properties of a material. It describes the dispersive properties of a dielectric medium, ***e.g.***, how its response changes with varying photon frequency.

Being a complex function of frequency, it can be expressed as follows: $\epsilon(\omega) = \epsilon_1(\omega) + i\epsilon_2(\omega)$. The real part, $\epsilon_1(\omega)$, is a measure of the dielectric constant of a dielectric material. It also defines the polarization of the material under an applied oscillating field. It also indicates the material's ability to store electrical energy in its electric field- a key feature of a dielectric material. It also describes light propagation in a dielectric material and thus measures the refractive index of a refracting material. The frequency-dependent imaginary part, $\epsilon_2(\omega)$, quantifies the energy loss to the incident light field propagating through a dielectric medium. In other words, it also indicates the material's ability to absorb energy from the oscillating applied field. This energy absorption leads to energy dissipation or attenuation. Alternatively, the light-matter interactions are responsible for these energy losses in a dielectric material. The stronger the light-matter interaction, the larger the energy dissipation in a dielectric medium. The higher the imaginary dielectric function, the greater the energy absorption from the incident light field (***e.g.***, the oscillating electric field). These energy losses also represent the loss tangent, defined as the ratio of the imaginary to the real dielectric constants of a material.

Theoretically, the imaginary dielectric function, $\epsilon_2(\omega)$, is estimated from the calculation of the matrix elements between the occupied and vacant energy states defined by the Fermi distribution function, while the Kramers-Kronig relation is used to calculate the real dielectric function, $\epsilon_1(\omega)$. These are given, in the linear optical approximation, as follows [59, 60],

$$\epsilon_2(\omega) = \frac{4\pi^2 e^2}{V m^2 \omega^2} \sum_{n,n'} \langle kn|p_i|kn'\rangle\langle kn'|p_j|kn\rangle \times f_{kn}(1 - f_{kn'})\, \delta(E_{kn'} - E_{kn} - E) \quad (6)$$

$$\epsilon_1(\omega) = 1 + \frac{2}{\pi} P \int_0^{\infty} \frac{\omega' \epsilon_2(\omega')\, d\omega'}{\omega'^2 - \omega^2} \quad (7)$$

In Eqs. (6) and (7), P is the principal value of the involved intergral, e is the electronic charge, V is the system's volume, m is the electron mass, ω is the oscillating frequency of the light field, $|kn\rangle$ is eigenket of the light propagation with the eigenvalue E_{kn}, the Fermi distribution function is denoted by f_{kn}, and E (= $\hbar\omega$) is the energy of the incident light field. The dielectric functions were calculated using the Kubo-Greenwood formula for the dielectric tensor as programmed in the OpenMX DFT simulation package discussed in Section 2 and described by Eqs. [6] and [7]. For the materials possessing hexagonal symmetry, only the diagonal terms, ***e.g.***, ϵ_{ii} (i=x, y, and z) in the dielectric tensor contribute to the total dielectric function; however, the off-diagonal terms, ***e.g.***, ϵ_{ij} (i, j=x, y, and z, with i≠j) are identically zero. These approximations are valid for the systems considered in this study because the 2D SiS_2 monolayer possesses a hexagonal symmetry. Additionally, the in-plane components contribute equally to the total dielectric function of a material with hexagonal symmetry. Moreover, the oscillating applied field is transverse. It carries two different polarization directions, ***e.g.***, in-plane (parallel, ||) and out-of-plane (perpendicular, ⊥). Therefore, the dielectric functions are estimated for field polarization parallel ($\epsilon^{||}$) and perpendicular ($\epsilon^{\perp}$) to the propagation direction. In the present case, we assumed that the material lies in the x-y plane. The dielectric function parallel to the field polarization direction (in-plane component) is denoted as $\epsilon^{||}_{xx}$ and $\epsilon^{||}_{yy}$, while the perpendicular component as $\epsilon^{\perp}_{zz}$ (with respect to the in-plane component). For all materials considered here, $\epsilon_{xx} = \epsilon_{yy}$ due to their hexagonal symmetry. Therefore, only the x-component of all quantities discussed in this work is considered.

The calculated dielectric functions (real and imaginary parts) of pure and doped SiS_2 materials are illustrated in Figure **5** for the varying frequency (ω) of the applied field. The dielectric and optical quantities illustrated in this work are plotted as a function of energy, ranging from 0 eV to 20 eV. The material's response in the visible region is indicated with a color bar in all figures. Also, the color description across all figures is preserved; ***e.g.***, black, red, blue, and pink indicate the response of pure (SiS_2-Pt@0%), SiS_2-Pt@3.70%, SiS_2-Pt@7.41%, and SiS_2-Pt@11.11%, see Figure **5**(**d**). Figures **5**(**a**) and **5**(**b**) elucidate the imaginary dielectric function. However, the average imaginary dielectric function is depicted in Figure **5**(**c**). The $\epsilon_2^{xx}(\omega)$ in pure the SiS_2 monolayer (SiS_2-Pt@0%) increases from zero with increasing photon frequency. The $\epsilon_2^{zz}(\omega)$ is zero in the visible region for a pure SiS_2 monolayer. With

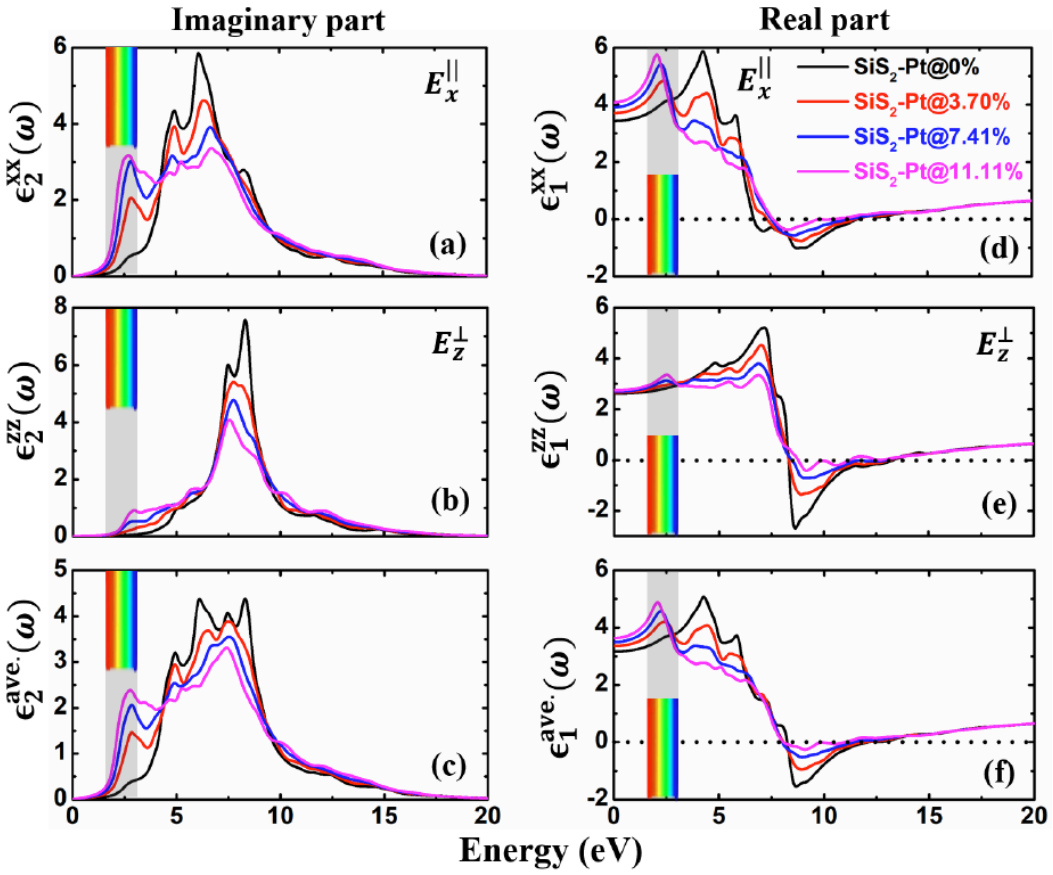

Figure 5: Dielectric functions of pure and doped SiS_2 monolayers at different doping level concentrations. (**a**) and (**b**) imaginary parts of the dielectric function in the x- and z-polarization directions. (**c**) The average imaginary dielectric function. (**d**) and (**e**) x- and z-components of the real dielectric function. (**f**) The average real dielectric function.

increasing photon frequency, several peaks and shoulders appear in the imaginary dielectric function. These peaks occur in the ultraviolet (UV) region along the x(z)-polarization direction and are centered around 4.91(7.5) eV and 6.0(8.3) eV, respectively, Figures **5**(**a**) and **5**(**b**). The z-component is larger than the x-component (between 3.70 eV and 10.0 eV) in a narrow UV energy region between 6.35 eV and 9.70 eV. These peaks correspond to electronic transitions between the filled VB and empty CB.

A significant increase in the x-component of $\epsilon_2(\omega)$ is seen in the visible region with increased doping concentration, Figure **5**(**a**). In contrast, the z-component is less affected due to doping. Simultaneously, doping remarkably reduces the imaginary dielectric function (parallel and perpendicular) in the ultraviolet (UV) region. A further reduction was observed with increasing Pt doping, Figure **5**(**a**). The x-component of ϵ_2 increases monotonically in the visible region. It is the maximum for all doped materials in a short energy interval between 1.80 eV and 2.85 eV in the visible region. These peaks indicate additional electronic transitions in the low-energy visible region, caused by the doping. Moreover, the decreased $\epsilon_2(\omega)$ in the UV region indicates that the number of overall electronic transitions reduces. The z-component also shows a significant decrease in the UV region with increasing doping concentration, as shown in Figure **5**(**a**). The average imaginary dielectric response of all materials is shown in Figure **5**(**c**). The average light response of all materials shows an overall increase in the imaginary dielectric function in the visible region and a corresponding decrease in the UV region after doping. It is responsible for the light-energy absorption, dissipation, or attenuation. Hence, the pure SiS_2 monolayer is an excellent UV light radiation absorber. However, it also partially absorbs incident radiation in the visible region in a noble metal Pt-atom-doped SiS_2 monolayer. This visible light absorption can be further enhanced by increasing the doping concentration. The pure material exhibits significant energy losses in the UV region. On the contrary, the doped materials show additional energy losses in the visible region. Simultaneously, losses in the UV region decrease after doping. Hence, the material behaves like a lossy medium.

The real dielectric functions in the x- and z-directions are depicted in Figures **5**(**c**) and **5**(**d**), respectively, with varying frequency of the incident light field. Its x-component increases smoothly with increasing incident light energy and attains a global

maximum value of 5.89 at 4.27 eV for SiS_2-Pt@0%, 4.83 at 2.40 eV for SiS_2-Pt@3.70%, 5.42 at 2.27 eV for SiS_2-Pt@7.41%, and 5.75 at 2.07 eV for SiS_2-Pt@11.11%, respectively. Beyond these energies, there is an overall decreasing trend of ϵ_1 found along the x-direction of the light polarization. It is the maximum for SiS_2-Pt@11.11% among all doped materials in the visible region. Simultaneously, its value significantly reduces in the UV region for all doped materials compared to the pure material. It indicates that the light polarization is improved in all doped materials in the visible region. However, it decreases in the UV region compared to the pure material. The x-component of the real dielectric function crosses below the zero value and approaches a finite negative value, indicating the metallic properties of the corresponding material. This means that the pure and doped materials are metallic at those energy values or energy ranges, as shown in Figures **5**(**d**) and **5**(**e**) for x- and z-components, respectively. The perfect conducting characteristic is due to the free movement of electronic charges, which cancel the electric field within the material. Moreover, a finite negative value of the real dielectric constant is also observed along the x-, Figure **5**(**d**), and z, Figure **5**(**e**), polarization directions. It signifies that the material is polarized in the opposite direction to the applied field, a feature not typically associated with naturally occurring materials [61, 62]. Materials with a negative real dielectric constant have potential applications in super and hyper-lenses, optical switches, and other novel thin-film-based optical components and devices. The doping has a less overall effect on the z-component. However, it slightly reduces polarization in the UV region compared to the pure material, Figure **5**(**e**). For higher frequencies, it is nearly unity for all materials. This means that doping has no significant role in higher energies. The average real dielectric constant is shown in Figure **5**(**f**). Most importantly, the static real dielectric constant, $\epsilon_1(0)$, is a fundamental material property that describes the material's polarization to store the electrical energy. The static real dielectric constant of SiS_2-Pt@0%, SiS_2-Pt@3.70%, SiS_2-Pt@7.41%, and SiS_2-Pt@11.11% along the x-polarization direction is 3.44, 3.72, 3.91, and 4.10, respectively. However, it is nearly 2.70 for all materials along the z-polarized axis. These findings indicate that the doped materials have a greater ability to be polarized and can store a large amount of energy in their electric field. Doping remarkably modifies the dielectric properties in the visible and UV regions. The energy losses increase and decrease in the visible and UV regions of the doped materials, exhibiting enhanced light absorption and material polarization in the visible region. It enhances the energy-storage ability of doped materials for low energies. These findings from the frequency-dependent dielectric function can be further correlated with optical parameters, including absorption and reflection coefficients, refractive index, and the loss function.

The obtained dielectric functions can be corroborated with the energy-loss function (ELF), which can be derived from them. It measures the energy losses of a wave traveling in the medium. The electron energy-loss spectrum indicates the interband electronic transitions in a material. The energy losses can be determined using electron energy-loss spectroscopy (EELS), a surface technique, in the light-matter interactions. It gives insights into how light interacts with the material. Light-matter interactions can lead to inelastic scattering of light waves from the material. This inelastic interaction between electrons in a material and light is responsible for the energy losses in the propagation medium. These occur in the low-energy incident light field and are mainly due to the excitation of valence electrons to the higher-energy unoccupied electronic states. These electronic excitations, from the filled VB to the unoccupied CB, are accompanied by plasmon oscillations. This leads to energy losses in a medium. These losses are related to the dielectric function of the medium. Moreover, the structural peaks in the dielectric functions correspond to peaks in the loss function. The energy loss function, $L(\omega)$, can be mathematically determined from the dielectric function as follows[63]:

$$L(\omega) = \frac{\epsilon_2(\omega)}{\epsilon_1^2(\omega)+\epsilon_2^2(\omega)} \quad (8)$$

All the symbols in Eq. (8) have their usual meanings.

The loss functions for the pure and doped SiS_2 monolayer materials along the x- and z-polarization directions are depicted in Figure **6**. Energy losses in the visible region are negligible along the z-polarized light, *e.g.*, doping has no effect on the EEL spectrum for light polarized in the perpendicular direction. A significant decrease in energy loss is observed between 13.0 eV and 15.0 eV in the z-direction, Figure **6**(**b**). This means that the maximum energy losses in the z-direction are in this energy range in the UV region. In particular, a sharp peak around 13.49 eV in the pure material corresponds to losses for higher energies. With a further increase in the doping concentration, the peak position shifts slightly and becomes broader. It indicates that the losses are slow for a range of energies. The energy loss in the doped SiS_2 monolayer increased below 5.0 eV along the x-direction. However, it was almost zero in the pure material, Figure **6**(**a**).

It corresponds to the plasma peak. Pure material shows a broad, small plasma peak centered around 5.0

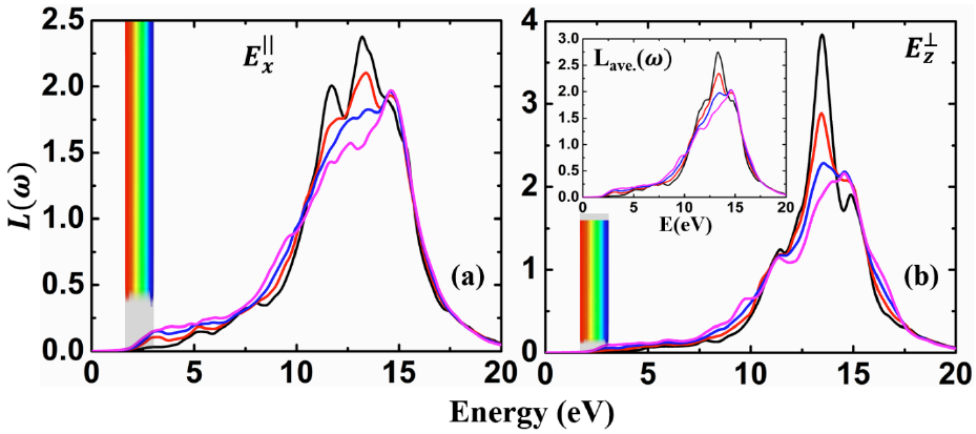

Figure 6: Electron energy loss, $L(\omega)$, in the light propagating in the pure and doped SiS2 monolayers along x-(**a**) and z-(**b**) electric field polarization directions, respectively. For color description, refer to Figure 5(**d**).

eV in the VUV region. Two other sharp peaks in the EEL spectrum of pure material were observed around 11.72 eV and 13.20 eV. The peak position and sharpness were reduced significantly in the highly doped SiS_2 monolayers. In the high-energy visible region, the losses increased in the doped material and were further enhanced with increasing doping concentration, Figure **6**(**a**). It follows peak positions at the end of the visible region in the imaginary dielectric function, Figure (**5**). The peaks in the EELS correspond to the energy losses in the medium. It shows that the material absorbs light at the respective energies. The larger energy loss corresponds to a smaller light transmission. Hence, less light penetration into the propagating medium implies light absorption. The average loss function is depicted in the inset of Figure (**6**). The energy losses in the low-energy region are due to the collective oscillations.

The $\epsilon_2(\omega)$ governs the light absorption (*e.g.*, attenuation of light waves). It is a physical phenomenon caused by the interaction of light with an absorbing medium. In light-matter interaction, the incident light is partially absorbed in the medium (the energy is transferred to the medium), and the rest is transmitted or reflected. The coefficient of absorption, $\alpha(\omega)$, measures the amount of light absorbed in the medium. However, the refractive index measures the light refraction. In other words, it indicates how the propagating material affects the direction and speed of light entering a dielectric material. In other words, it is an optical quantity that measures how a material responds after interacting with light. It is fundamentally important to understand the manipulation of light behavior for different optical applications. It is a material-dependent optical property; therefore, it is useful for characterizing and identifying different materials. The abortion coefficient, $\alpha(\omega)$, and refractive index, $n(\omega)$, can theoretically be calculated from the real and imaginary parts of the dielectric function using the following relations,

$$\alpha(\omega) = \frac{\sqrt{2}\,\omega}{c}\left[\sqrt{\epsilon_1^2(\omega) + \epsilon_2^2(\omega)} - \epsilon_1(\omega)\right]^{\frac{1}{2}} \quad (9)$$

$$n(\omega) = \frac{1}{\sqrt{2}}\left[\sqrt{\epsilon_1^2(\omega) + \epsilon_2^2(\omega)} + \epsilon_1(\omega)\right]^{\frac{1}{2}} \quad (10)$$

Where the parameters have their usual meaning. These quantities in pure and Pt-atom-doped SiS_2 monolayer are illustrated in Figure **7** along both polarization directions. As discussed above, the imaginary part of the dielectric function is responsible for light absorption. Therefore, the line and shape of the absorption coefficient are expected to be similar. Figure **7**(**a**) illustrates the light absorption, specifically the x-component. All materials exhibit a strong UV light absorption. Therefore, these are excellent absorbers of UV radiation. The absorption peaks between 6.0 eV and 9.0 eV are consistent with those in the imaginary dielectric function, Figure **5**(**a**). The absorption coefficient in the z-polarized direction is greater than in the x-direction. It shows a significant decrease in all the doped materials in the UV region. As the doping concentration increases, the UV light absorption continuously decreases in both polarization directions. Moreover, the increased doping concentration significantly enhances light absorption in the visible region, particularly for violet light. Simultaneously, the threshold of light absorption shifted towards the lower energy. These observations align with the estimated imaginary part of the dielectric function. Besides that, the absorption spectrum behaves differently along the x- and z-directions of the light polarization. It signifies that the absorption spectrum is propagation-direction-dependent. In other words, it is anisotropic with respect to light polarization directions. Anisotropic absorption spectra may arise for several reasons, such as anisotropic crystal structure caused by the different arrangements of atoms or molecules along different directions, the material's structure itself, and the

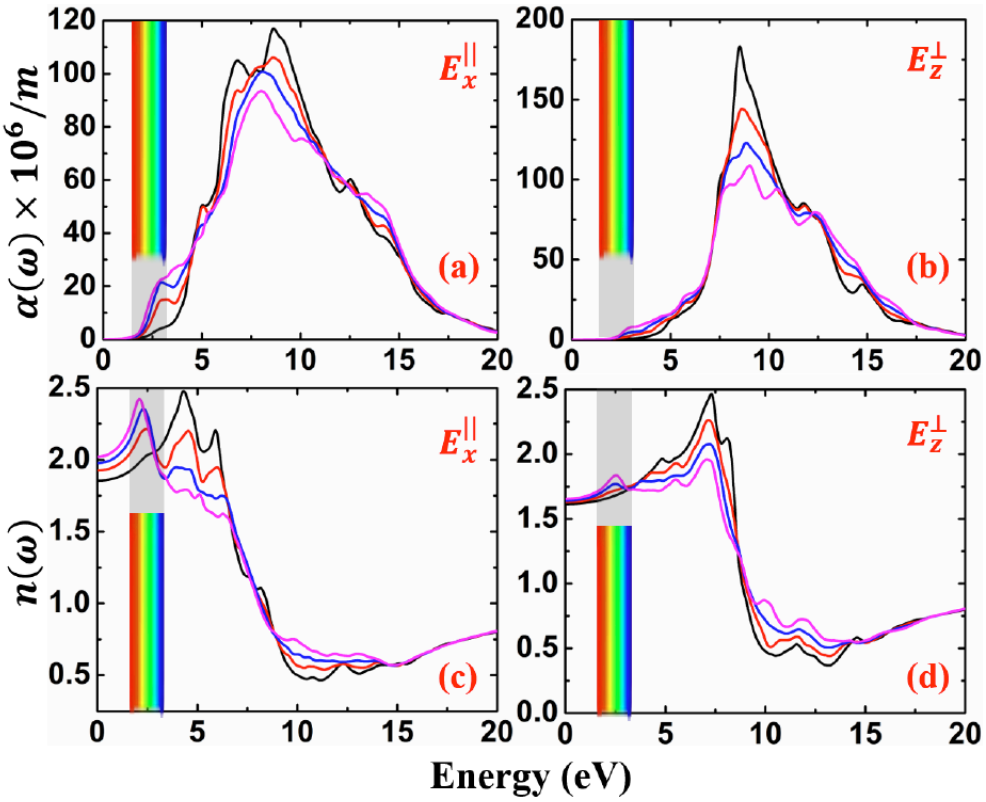

Figure 7: Absorption coefficient and refractive index in the pure and doped SiS_2 monolayers. (**a**) and (**b**) absorption of light along x- and z-light field polarization directions. (**c**) and (**d**) refractive indices of pure and doped materials along x- and z-light field polarization directions.

direction of light incidence and orientation of the material. Anisotropic absorption spectra make these materials useful for specific optical applications such as photovoltaics, optical polarization filters, and polarization-sensitive electronic and optical devices. The polarization-dependent light absorption in SiS_2 can be used to build on-chip polarizers and polarization-sensitive photodetectors, which are solely attributable to its anisotropy that preferentially absorbs light based on its polarization state. This enables the creation of filter-free, miniaturized, and highly integrated devices for applications in optical communications, sensing, and imaging. A polarization-sensitive photodetector converts the difference in polarization-dependent absorption directly into a measurable electrical signal. The device's response is highest for one polarization and lowest for the orthogonal polarization, resulting in a high polarization ratio.

Light waves deviate from their original path when passing from one medium to another. This phenomenon is called the refraction (*e.g.*, bending) of light. This bending of light is due to the different densities of the two materials. It is the intrinsic property of a material and is wavelength-dependent. The index of refraction is known as the refractive index, $n(\omega)$, and measures how fast the light travels into the material. Generally, it is a complex quantity because, when light passes through a medium, it is partially absorbed in that medium. The real part is called the refractive index, and the imaginary part is responsible for the light extinction (discussed later). The refractive index is a material- and wavelength-dependent property of a medium. It also depends on the polarization directions. The refractive indices of the materials considered are displayed in Figure **7**. The z-component of the refractive index in the visible region almost remains the same for all materials, Figure **7**(**b**). However, it decreases along both polarized directions with increasing doping concentration in the VUV region. In the visible region, the x-component increases with the doping concentration. Also, it increases smoothly with increasing photon frequency and reaches a maximum for a highly Pt-doped material. Hence, it exhibits maximum light polarization in the visible region and can store a large amount of energy in its electric field. Most important is its static refractive index, $n(0)$- the refractive index at zero photon frequency or a specific wavelength. The maximum refractive indices of doped materials in the visible region along the x-direction are 2.22 at 2.45 eV in SiS_2-Pt@3.70%, 2.35 at 2.32 in < SiS_2-Pt@7.41%, and 2.43 at 2.10 in SiS_2-Pt@11.11%. However, the refractive index of the pure material (SiS_2-Pt@0%) along the x-direction is a maximum of 2.48 at 4.32 eV. Moreover, the refractive indices of SiS_2-Pt@0%, SiS_2-Pt@3.70%, SiS_2-Pt@7.41%, and SiS_2-Pt@11.11% at zero photon

frequency along the x-direction are 1.85, 1.92, 1.98, and 2.02, respectively. These are greater and smaller than sapphire (n~1.77) and zirconia (n~2.15). This means the static refractive index of pure material improves significantly after doping and increases with increasing doping concentration. In other words, the x-component of the refractive index increases with increasing doping concentration. Simultaneously, it shows a decrease in the VUV region with increasing Pt-concentration. Moreover, these materials have a refractive index below one in the high-energy region (>8.0 eV). This means that these materials are useful for long-distance radio wave communications. Besides that, the refractive index has a different behavior along the x- and z-polarization directions. It suggests that these materials exhibit an anisotropic refractive index. Hence, these materials are optically anisotropic, showing their potential in anisotropic optoelectronic devices.

The light absorption properties of optical materials can also be estimated from the extinction or attenuation coefficient. It is the attenuation of electromagnetic radiation traversing a material medium. It is a quantitative measure of how light photons interact with the electrons in a light-absorbing material, thereby influencing absorption properties. It describes a decrease in the intensity of electromagnetic radiation propagating through a material medium, caused by light scattering (a change in the direction of light) or absorption by the atoms or molecules in the absorbing medium. Alternatively, it is a characteristic property that describes how strongly a medium absorbs or reflects the incident light. This property of an absorbing material is used in different fields of science. Specifically, it is used to model and manipulate the propagation direction of light in several media. For instance, air and water, as well as other condensed phases of matter.

The calculated extinction coefficient versus the photon energy is illustrated in Figure **8**. On comparing Figures **8**(**a**) and **8**(**b**), it is noticed that the overall light extinction is maximum in the UV region along the z-polarized direction, indicating strong light-matter interaction. It also signifies the fast light absorption by electrons and atoms in the absorbing material, leading to a maximum absorption coefficient for the respective incident radiation or a particular wavelength of light. In other words, the energy region corresponding to the maximum extinction coefficient resembles a maximum light absorption or attenuation. It follows the observed imaginary dielectric function, emphasizing its role in determining the absorption, extinction, or attenuation. A significant decrease in both components of the extinction coefficient is observed with increasing doping concentration in the UV region, as shown in Figures **8**(**a**) and **8**(**b**). However, the extinction coefficient increases with increasing doping concentration in the visible region. It shows a

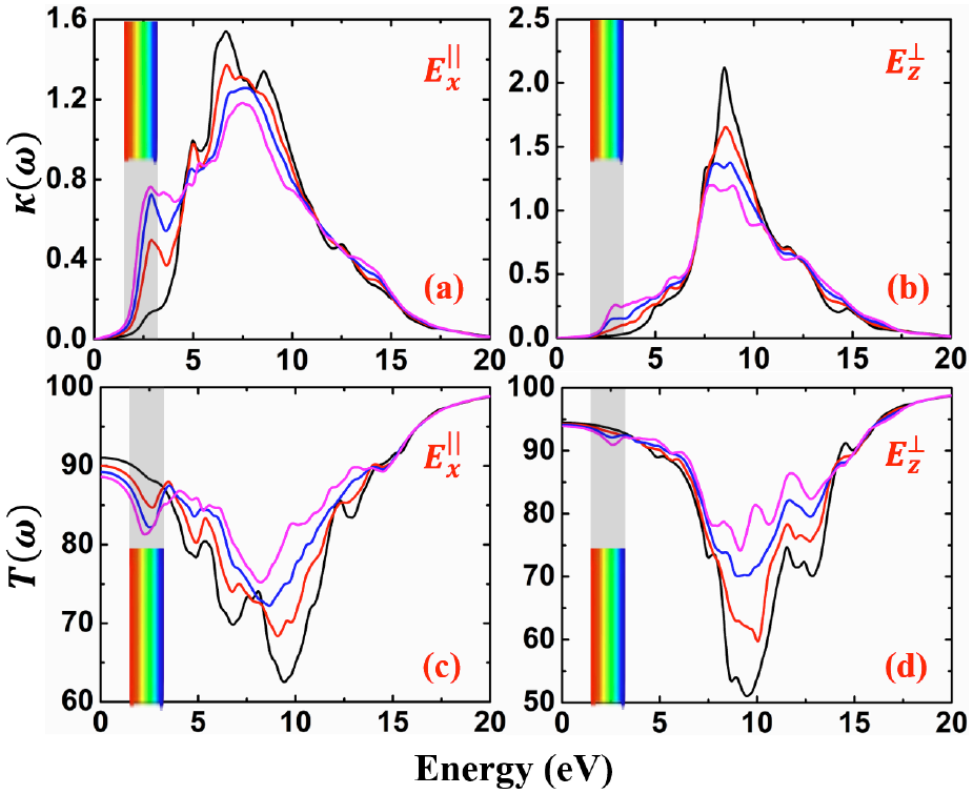

Figure 8: Extinction and transmission coefficients in pure and doped SiS_2 monolayer materials. (**a**) and (**b**) extinction coefficient. (**c**) and (**d**) light transmission coefficient.

remarkable enhancement in the visible region and reaches a maximum at an 11.11% Pt-doping concentration. Its rising edge shifted toward lower energy as the doping percentage increased from 0% to 11.11%. It supports the observed absorption spectra: *e.g*., increased light extinction corresponds to enhanced light absorption in the medium. These findings emphasize that the imaginary dielectric function, absorption spectra, and extinction coefficient are mutually consistent.

The extinction coefficient indicates the amount of light absorption or reflection. A higher absorption or extinction corresponds to the light traveling a shorter distance in the medium, suggesting that the light penetrates a lesser distance in the material medium. Hence, the penetration depth in a material medium is less. In other words, less light penetration corresponds to a small light transmission through the material. Therefore, the rising edges in the extinction coefficient correspond to the trailing edges in the corresponding transmission spectra. It emphasizes the increasing trend of the extinction coefficient, Figures **8**(**a**) and **8**(**b**) reflect a decreasing trend in the corresponding transmission spectra, Figures **8**(**c**) and **8**(**d**), respectively. A decrease in the light transmission indicates the increased light reflection from the propagating medium. The corresponding reflection spectrum is depicted in Figure **S7** of the **SI**. The overall light transmission (reflection) increased (decreased) in the UV region. However, the transmission is slightly decreased in the visible region, with a corresponding effect on the reflection spectra. The reflection of light can be further reduced by increasing the doping concentration, as shown in Figures **S7**(**a**) and **S7**(**b**). Hence, the corresponding light transmission increased, suggesting the reduced light-matter interaction. The static transmission coefficient is nearly 90% and 95% along the x- and z-axes. Hence, these are good candidates for polarized transmission filters in the low-energy visible and VUV regions.

3.3. Scintillation Properties: Light Yield Estimation

A material or compound that converts radiation energy into visible light is called a scintillating material. These materials have a crucial role in all high-energy radiation detectors. Inorganic scintillating materials and detectors have various applications in fields such as imaging and diagnosis, high-energy physics, and security. Several inorganic scintillating materials and detectors have been reviewed in refs. [38, 64, 65]. Recently, halide perovskite materials have gained significant research interest their scintillation properties [66, 67]. Given the above, scientists have also recently investigated the family of 2D perovskite materials to study their properties for ionizing radiation detection [68]. These studies motivate us to investigate whether these materials are suitable for detecting ionizing radiation. Here, it is worth noting that an excellent scintillating material combines several optical characteristics, such as a high refractive index and transmission rate. A good scintillating material also possesses low reflectivity and a low absorption coefficient in its emission range. The materials met these requirements at the ends of the visible and UV regions, respectively. Therefore, we also estimated the upper light yield, LY_{SC}, in these materials, which is the most important property of a scintillator. Materials with high upper light yield can detect low-energy radiations (intensities) because they have a high signal-to-noise (S/N) ratio. It determines the number of emitted scintillated photons per MeV of radiation energy and measures its performance [38]. The output light yield can be estimated using a phenomenological model that describes a scintillator's performance. A detailed discussion of the phenomenological model for estimating the output light yield can be found in the refs. [69-72]. We calculated the output light yield with the simplified form of the phenomenological model that was used to estimate the scintillation performance of $TlMgCl_3$ [43] and Cs_2KSnX_6(X=Cl, Br, and I) [44], given below

$$LY_{SC} = \frac{S \times Q}{\beta E_g} \times 10^6 \text{ photons/MeV} \quad (11)$$

Where S indicates the energy transfer efficiency to the activators, Q is the quantum efficiency, β is a constant parameter, and E_g is the band gap of a scintillating material. The product βE_g is the energy required to generate an electron-hole (e-h) pair. It is obvious from Eq. (11) that the output light yield is inversely proportional to the band gap. Therefore, the light output yield in a material with a narrow band gap is higher than in wide band gap materials.

In ionic materials, β is smaller (between 1.5 and 2.0). The high value of β (between 3.0 and 4.0) in covalent materials causes more energy losses and less output light yield. The β value was fixed at 2.5 according to theoretical and experimental studies on several scintillating materials [38]. The energy losses in scintillators and β values were reviewed by Rodnyi *et al*. [71]. Theoretical and experimental studies have reported $\beta \approx 3$ for semiconductors with a band gap (between 0.7 eV and 3.0 eV) and a wide valence band [73]. However, it is between 2.0 and 3.0 for materials with a wide band gap [71]. Due to thermalization, the β value is higher for semiconductors than for ionic crystals. It is due to the energy loss that occurs during the thermalization of electrons and holes in a semiconductor. However, the electron thermalization is predominant in the ionic crystals. If it is assumed that all charge carriers are transferred to the activator (*e.g*., S=1), and the quantum efficiency of the activator is

Table 5: Output light yield, LY_{SC}, Estimation in Pure and Doped SiS_2 Monolayers. It is Expressed in Units of Photons/MeV

System	SiS_2-Pt@0%	SiS_2-Pt@3.70%	SiS_2-Pt@7.41%	SiS_2-Pt@11.11%
LY_{SC}	281690	223464	222222	217980

unity (*e.g.*, Q=1). Then, the fundamental limit on the light output of a scintillator can be solely estimated from the number of e-h pairs generated in the ionizing track, and can be expressed as follows [70],

$$N_{e-h} = \frac{E_\gamma}{\beta E_g} \text{ photons/MeV} \quad (12)$$

Where, E_γ is the energy of the ionization radiation. According to Eq. (12), a large number of e-h pairs can be generated in a scintillating material with a small band gap and vice versa. The scintillating performance of a few halide-based materials has been studied using the $\gamma-$ionizing radiation [43, 44]. Following these studies, the calculated light yields for the pure and doped SiS_2 materials are listed in Table **5**.

The reported values represent the upper limit of the output light yield under ideal conditions, which is achievable with scintillating materials. The light yield under ideal conditions is maximum for the pure material (SiS_2-Pt@0%) because its absorption coefficient is lower than that of the doped materials in the visible and near UV regions. The decline in light absorption is a fundamental feature that significantly improves the overall performance of a scintillator, as high light absorption leads to increased losses from these materials. The light yield may be further reduced by internal reflections in a scintillating material. Due to these internal reflections, not all charges are reaching the detector. It leads to a decreased detection of created scintillating photons (*e.g.*, $S < 1$). Additionally, the decrease in the upper limit of output light yield may be attributed to the presence of trapped electron-hole pairs at crystal defects or surface states. These reasons may lead to a decrease in light yield in doped SiS_2 materials. The reported value of the output light yield in these materials is significantly larger than the estimated value in a wide band gap $TlMgCl_3$ material [43] and smaller than that in a few halide perovskites [44]. A light yield of 281,690 photons/MeV represents the scintillating efficiency of the SiS_2 monolayer in converting ionizing radiation energy into light. This numerical value means that approximately 281690 photons of light can be produced from every one MeV of energy deposited in the material by a particle. Our estimated light yields for the studied materials indicate they are excellent scintillators for radiation detection applications. Hence, the SiS_2 monolayer may be a potential candidate for applications such as high-energy physics, diagnosis, imaging, and security. Moreover, this is the first study to investigate the scintillation properties of the SiS_2 monolayer. A rigorous experimental study is necessary to validate these results and investigate the potential mechanisms for energy losses in these scintillating materials.

4. CONCLUSIONS

This work investigated the optoelectronic properties of a noble-metal-doped SiS_2 monolayer using density functional theory. The scintillation properties of these materials have also been examined and briefly discussed. The calculated electronic band structure and density of states (DOS) reveal the indirect band gap feature of these materials. The obtained band gap in the pure SiS_2 monolayer is nearly 1.42 eV, which agrees with the reported values. Doping led to a significant change in its electronic properties. For example, the band gap in the 3.70% Pt-doped SiS_2 monolayer is significantly higher than that of the pure form. Moreover, increasing the doping concentration slightly changes its band gap. These findings have been supported by the calculated DOS in these materials. The estimated HOMO-LUMO gap is fundamental in determining the material's kinetic stability and chemical reactivity. It is found that a pure material possesses high hardness, chemical stability, and less chemical reactivity. However, the softness of the material increases with increasing doping concentration and becomes more chemically reactive. Noble-metal doping alters the material's electronic properties, thereby changing its optical response. Therefore, we reported frequency-dependent dielectric and optical parameters, including dielectric functions, absorption and transmission coefficients, index of refraction, and energy losses. It is observed that doping significantly enhances light absorption in the visible region, while it decreases in the ultraviolet (UV) region. An increased and decreased imaginary dielectric function in the visible and UV regions, caused by Pt-doping, is consistent with the observed absorption spectrum in these materials. The energy losses in a dielectric material are due to light absorption. The obtained light absorption is polarization-dependent, which can be utilized to build on-chip polarizers and polarization-sensitive photodetectors. This enables the creation of filter-free, miniaturized, and highly integrated devices for applications in optical

communications, sensing, and imaging. Moreover, the calculated real dielectric function is negative- a feature not typically associated with naturally occurring materials, indicating that the material exhibits metallic characteristics at those energies. Materials with a negative real dielectric constant have potential applications in super and hyper-lenses, optical switches, and other novel thin-film-based optical components and devices. Stronger light absorption corresponds to the maximum in the energy-loss spectrum, indicating stronger light attenuation in the corresponding energy range. The refractive index of the doped materials is enhanced significantly in the visible region. The obtained static refractive indexes of SiS_2-Pt@0%, SiS_2-Pt@3.70%, SiS_2-Pt@7.41%, and SiS_2-Pt@11.11% are 1.85, 1.92, 1.98, and 2.02, respectively. Moreover, the estimated dielectric and optical quantities exhibit different behavior along different directions, indicating an anisotropic optical response in these materials. Hence, these materials may be useful for realizing anisotropic, polarization-dependent optoelectronic devices. Additionally, these materials are exµcellent scintillators for detecting high-energy ionizing radiation. The estimated output light yield is slightly higher for an undoped material than for a doped one. The excellent optoelectronic and scintillating properties indicate that the thin films of the studied material are potential candidates for optoelectronic devices and high-energy physics, including security, imaging, and diagnosis.

CONFLICTS OF INTEREST

The authors declare that they have no conflicts of interest.

REFERENCE

[1] K.S. Novoselov, A.K. Geim, S. V. Morozov, D. Jiang, Y. Zhang, S. V. Dubonos, I. V. Grigorieva, A.A. Firsov, Electric Field Effect in Atomically Thin Carbon Films, Science (80). 306 (2004) 666. https://doi.org/10.1126/science.1102896

[2] L. Jiang, D. Zhou, J. Yang, S. Zhou, H. Wang, X. Yuan, J. Liang, X. Li, Y. Chen, H. Li, 2D single- and few-layered MXenes: synthesis, applications and perspectives, J. Mater. Chem. A. 10 (2022) 13651-13672. https://doi.org/10.1039/D2TA01572B

[3] J. Nam, G.Y. Lee, D.Y. Lee, D. Sung, S. Hong, A.R. Jang, K.S. Kim, Tailored Synthesis of Heterogenous 2D TMDs and Their Spectroscopic Characterization, Nanomaterials. 14 (2024). https://doi.org/10.3390/mi14122139

[4] S. Madhurantakam, G. Mathew, B.E. David, A. Naqvi, S. Prasad, Recent Progress in Transition Metal Dichalcogenides for Electrochemical Biomolecular Detection, Micromachines. 14 (2023). https://doi.org/10.1021/acs.jpcc.5b02950

[5] F.A. Rasmussen, K.S. Thygesen, Computational 2D Materials Database: Electronic Structure of Transition-Metal Dichalcogenides and Oxides, J. Phys. Chem. C. 119 (2015) 13169-13183.

[6] S. Balendhran, S. Walia, H. Nili, S. Sriram, M. Bhaskaran, Elemental analogues of graphene: Silicene, germanene, stanene, and phosphorene, Small. 11 (2015) 640-652. https://doi.org/10.1002/smll.201402041

[7] K. Momeni, Y. Ji, Y. Wang, S. Paul, S. Neshani, D.E. Yilmaz, Y.K. Shin, D. Zhang, J.W. Jiang, H.S. Park, S. Sinnott, A. van Duin, V. Crespi, L.Q. Chen, Multiscale computational understanding and growth of 2D materials: a review, Npj Comput. Mater. 6 (2020). https://doi.org/10.1038/s41524-020-0280-2

[8] P. Miró, M. Audiffred, T. Heine, An atlas of two-dimensional materials, Chem. Soc. Rev. 43 (2014) 6537. https://doi.org/10.1039/C4CS00102H

[9] B.N. Nguyen Thi, C.V. Ha, N. Thi Ha Lien, J. Guerrero-Sanchez, D.M. Hoat, Doping-mediated electronic and magnetic properties of graphene-like ionic NaX (X = F and Cl) monolayers, Phys. Chem. Chem. Phys. 25 (2023) 32569-32577. https://doi.org/10.1039/D3CP02115G

[10] J. Zhou, L. Shen, M.D. Costa, K.A. Persson, S.P. Ong, P. Huck, Y. Lu, X. Ma, Y. Chen, H. Tang, Y.P. Feng, 2DMatPedia, an open computational database of two-dimensional materials from top-down and bottom-up approaches, Sci. Data. 6 (2019) 1-10. https://doi.org/10.1038/s41597-018-0005-2

[11] Y. Wei, H. Liu, K. Wang, Magnetic anisotropy and phononic properties of two-dimensional ferromagnetic Fe3GeS2 monolayer, IScience. 27 (2024) 110781. https://doi.org/10.1016/j.isci.2024.110781

[12] D.B. Long, L.M. Yang, Transmutation Engineering Makes a Large Class of Stable and Exfoliable A3BX2 Compounds with Exceptional High Magnetic Critical Temperatures and Exotic Electronic Properties, ACS Appl. Mater. Interfaces. 15 (2023) 24549-24569. https://doi.org/10.1021/acsami.3c02536

[13] https://en.wikipedia.org/wiki/2D_Materials, (n.d.).

[14] B. Aktekin, L.M. Riegger, S.K. Otto, T. Fuchs, A. Henss, J. Janek, SEI growth on Lithium metal anodes in solid-state batteries quantified with coulometric titration time analysis, Nat. Commun. 14 (2023). https://doi.org/10.1038/s41467-023-42512-y

[15] E.C. Ahn, 2D materials for spintronic devices, Npj 2D Mater. Appl. 4 (2020). https://doi.org/10.1038/s41699-020-0152-0

[16] M.V. Sulleiro, A. Dominguez-Alfaro, N. Alegret, A. Silvestri, I.J. Gómez, 2D Materials towards sensing technology: From fundamentals to applications, Sens. Bio-Sensing Res. 38 (2022). https://doi.org/10.1016/j.sbsr.2022.100540

[17] L. Tang, X. Meng, D. Deng, X. Bao, Confinement Catalysis with 2D Materials for Energy Conversion, Adv. Mater. 31 (2019) 1-16. https://doi.org/10.1002/adma.201901996

[18] J. An, X. Zhao, Y. Zhang, M. Liu, J. Yuan, X. Sun, Z. Zhang, B. Wang, S. Li, D. Li, Perspectives of 2D Materials for Optoelectronic Integration, Adv. Funct. Mater. 32 (2022) 1-24. https://doi.org/10.1002/adfm.202110119

[19] M. Long, P. Wang, H. Fang, W. Hu, Progress, Challenges, and Opportunities for 2D Material Based Photodetectors, Adv. Funct. Mater. 29 (2019) 1803807. https://doi.org/10.1002/adfm.201803807

[20] W.O. Razmus, K. Acheson, P. Bucksbaum, M. Centurion, E. Champenois, I. Gabalski, M.C. Hoffman, A. Howard, M.F. Lin, Y. Liu, P. Nunes, S. Saha, X. Shen, M. Ware, E.M. Warne, T. Weinacht, K. Wilkin, J. Yang, T.J.A. Wolf, A. Kirrander, R.S. Minns, R. Forbes, Multichannel photodissociation dynamics in CS2 studied by ultrafast electron diffraction, Phys. Chem. Chem. Phys. 24 (2022) 15416-15427. https://doi.org/10.1039/D2CP01268E

[21] H. Ullah, M. Noor-A-Alam, Y. Shin, Vacancy and doping-dependent electronic and magnetic properties of monolayer SnS2, J. Am. Chem. Soc. 103 (2020) 391-402. https://doi.org/10.1111/jace.16739

[22] X. Dong, T.A. Pham, C. Xu, Y. He, W. Lai, X. Ke, P. Zhang, Growth and Electronic Properties of SnSe2 Films on Reconstructed, (111)-Oriented SrTiO3 Substrates, J. Phys. Chem. C. 127 (2023) 16732-16739. https://doi.org/10.1021/acs.jpcc.3c04609

[23] L.A. Burton, T.J. Whittles, D. Hesp, W.M. Linhart, J.M. Skelton, B. Hou, R.F. Webster, G. O'Dowd, C. Reece, D. Cherns, D.J. Fermin, T.D. Veal, V.R. Dhanak, A. Walsh, Electronic and optical properties of single crystal SnS2: An earth-abundant disulfide photocatalyst, J. Mater. Chem. A. 4 (2016) 1312-1318. https://doi.org/10.1039/C5TA08214E

[24] G. Tse, The structural, electronic, optical, elastic, and vibrational properties of GeS2 using HSE03: a first-principle investigation Published: 06 July 2024, J. Comput. Electron. 23 (2024) 968-976. https://doi.org/10.1007/s10825-024-02196-z

[25] R. Mishra, P.K. Mishra, S. Phapale, P.D. Babu, P.U. Sastry, G. Ravikumar, A.K. Yadav, Evidences of the existence of SiTe2 crystalline phase and a proposed new Si-Te phase diagram, J. Solid State Chem. 237 (2016) 234-241. https://doi.org/10.1016/j.jssc.2016.02.021

[26] Y. Wang, L.M. Vu, T. Lu, C. Xu, Y. Liu, J.Z. Ou, Y. Li, Piezoelectric Responses of Mechanically Exfoliated Two-Dimensional SnS2Nanosheets, ACS Appl. Mater. Interfaces. 12 (2020) 51662-51668. https://doi.org/10.1021/acsami.0c16039

[27] R. Gao, Y. Yong, X. Yuan, S. Hu, Q. Hou, Y. Kuang, First-Principles Investigation of Adsorption Behaviors and Electronic, Optical, and Gas-Sensing Properties of Pure and Pd-Decorated GeS2Monolayers, ACS Omega. 7 (2022) 46440-46451. https://doi.org/10.1021/acsomega.2c05142

[28] Y. Liu, W. Li, F. Li, Z. Chen, Computational discovery of diverse functionalities in two-dimensional square disulfide monolayers: auxetic behavior, high curie temperature ferromagnets, electrocatalysts, and photocatalysts, J. Mater. Chem. A. 11 (2023) 20254-20269. https://doi.org/10.1039/D3TA03699E

[29] H. Wang, T. Li, Z. Chen, W. Zhu, W. Lin, H. Wang, X. Liu, Z. Li, High out-of-plane negative Poisson's ratios and strong light harvesting in two-dimensional SiS2 and its derivatives, Nanoscale. 15 (2023) 16155-16162. https://doi.org/10.1039/D3NR04483A

[30] D. Plašienka, R. Martoňák, E. Tosatti, Creating new layered structures at high pressures: SiS2, Sci. Rep. 6 (2016) 1-11. https://doi.org/10.1038/s41598-016-0001-8

[31] J. Evers, L. Möckl, G. Oehlinger, R. Köppe, H. Schnöckel, O. Barkalov, S. Medvedev, P. Naumov, More Than 50 Years after Its Discovery in SiO2 Octahedral Coordination Has Also Been Established in SiS2 at High Pressure, Inorg. Chem. 56 (2017) 372-377. https://doi.org/10.1021/acs.inorgchem.6b02294

[32] M. Naseri, M. Abutalib, M. Alkhambashi, J. Gu, J. Jalilian, A. Farouk, J. Batle, Prediction of novel SiX2(X = S, Se) monolayer semiconductors by density functional theory, Phys. E Low-Dimensional Syst. Nanostructures. 114 (2019) 113581. https://doi.org/10.1016/j.physe.2019.113581

[33] X. Wang, L. Wang, Y. Li, Prediction of SiS2 and SiSe2 as promising anode materials for sodium-ion batteries, Phys. Chem. Chem. Phys. 24 (2022) 13189-13193. https://doi.org/10.1039/D2CP01184K

[34] Y. Guan, X. Li, R. Niu, N. Zhang, T. Hu, L. Zhang, Tunable electronic properties of type-ii sis2/wse2 hetero-bilayers, Nanomaterials. 10 (2020) 1-11. https://doi.org/10.3390/nano10102037

[35] Q.Y. Chen, M.Y. Liu, C. Cao, Y. He, Strain-dependent optical properties of the novel monolayer group-IV dichalcogenides SiS2semiconductor: A first-principles study, Nanotechnology. 32 (2021). https://doi.org/10.1088/1361-6528/abeada

[36] W.J. Zhao, L. Ma, L.C. Ma, X.H. Tian, J.M. Zhang, First-principles study on the photocatalytic property of SiS/BSe and SiS2/BSe van der Waals heterojunctions, Eur. Phys. J. B. 96 (2023) 1-17. https://doi.org/10.1140/epjb/s10051-022-00470-2

[37] Piotr A Rodnyi, Physical Processes in inorganic scintillators, 1st Editio, CRC Press, Boca Raton New York, 1997.

[38] T. Yanagida, Inorganic scintillating materials and scintillation detectors, Proc. Jpn. Acad., Ser. B. 94 (2018) 75-97. https://doi.org/10.2183/pjab.94.007

[39] P. Lecoq, A. Gektin, M. Korzhik, Inorganic Scintillators for Detector Systems, Physical Principles and Crystal Engineering, Second Edi, Springer, Cham Switzerland, 2017. https://doi.org/10.1007/978-3-319-45522-8

[40] Y. Fujimoto, M. Koshimizu, T. Yanagida, G. Okada, K. Saeki, K. Asai, Thallium magnesium chloride: A high light yield, large effective atomic number, intrinsically activated crystalline scintillator for X-ray and gamma-ray detection, Jpn. J. Appl. Phys. 55 (2016) 4-7. https://doi.org/10.7567/JJAP.55.090301

[41] T. Yanagida, Y. Fujimoto, M. Arai, M. Koshimizu, T. Kato, D. Nakauchi, N. Kawaguchi, Comparative studies of scintillation properties of Tl-based crystals, Sensors Mater. 32 (2020) 1351-1356. https://doi.org/10.18494/SAM.2020.2711

[42] S.U. Zaman, N. Rahman, M. Arif, M. Saqib, M. Husain, E. Bonyah, Z. Shah, S. Zulfiqar, A. Khan, Ab initio investigation of the physical properties of Tl based chloroperovskites TlXCl3(X = Ca and Cd), AIP Adv. 11 (2021). https://doi.org/10.1063/5.0034759

[43] M.N. Murshed, M.E. El Sayed, S. Naji, A. Samir, Electronic and optical properties and upper light yield estimation of new scintillating material TlMgCl3: Ab initio study, Results Phys. 29 (2021) 104695. https://doi.org/10.1016/j.rinp.2021.104695

[44] M.A. Javed, R. Ahmed, S.A. Tahir, B. Ul Haq, Investigations of optoelectronic and scintillating properties of novel halide perovskites Cs2KSnX6 (X=Cl, Br, I), J. Solid State Chem. 341 (2025) 125084 (and refereces therein). https://doi.org/10.1016/j.jssc.2024.125084

[45] N.H. Linh, T.T. Quang, N.M. Son, V. Van Thanh, D. Van Truong, Prediction of mechanical, electronic and optical properties of monolayer 1T Si-dichalcogenides via first-principles theory, Mater. Today Commun. 36 (2023) 106553. https://doi.org/10.1016/j.mtcomm.2023.106553

[46] N.T. Han, J. Guerrero-Sanchez, D.M. Hoat, Pnictogen Atom Substitution to Modify the Electronic and Magnetic Properties of SiS2 Monolayer: A DFT Study, Adv. Theory Simulations. 2400900 (2024) 1-11.

[47] D. B. Long, N. V. Tkachenko, Q. Feng, X. Li, A.I. Boldyrev, J. Yang, L.-M. Yang, Two-dimensional Bimetal-Embedded Expanded Phthalocyanine Monolayers: A Class of Multifunctional Materials with Fascinating Properties, Adv. Funct. Mater. (2024) 2313171-10.

[48] D.B. Long, Y. Feng, G. Gao, L.M. Yang, Effective modulation of the exotic properties of two-dimensional multifunctional TM2@g-C4N3 monolayers via transition metal permutation and biaxial strain, Nanoscale. 15 (2023) 9843-9863. https://doi.org/10.1039/D3NR00984J

[49] C. Wang, L.M. Yang, Alkaline-earth metal embedded expanded phthalocyanine nanosheets with direct band gaps and high power conversion efficiency, J. Mater. Chem. C. 12 (2024) 10181-10192. https://doi.org/10.1039/D4TC01541J

[50] C.C. Lee, Y.T. Lee, M. Fukuda, T. Ozaki, Tight-binding calculations of optical matrix elements for conductivity using nonorthogonal atomic orbitals: Anomalous Hall conductivity in bcc Fe, Phys. Rev. B. 98 (2018) 1-8. https://doi.org/10.1103/PhysRevB.98.115115

[51] Y.T. Lee, C.C. Lee, M. Fukuda, T. Ozaki, Unfolding optical transition weights of impurity materials for first-principles LCAO electronic structure calculations, Phys. Rev. B. 102 (2020) 1-9. https://doi.org/10.1103/PhysRevB.102.075143

[52] X. Ge, X. Zhou, D. Sun, X. Chen, First-Principles Study of Structural and Electronic Properties of Monolayer PtX2 and

Janus PtXY (X, Y = S, Se, and Te) via Strain Engineering, ACS Omega. 8 (2023) 5715-5721. https://doi.org/10.1021/acsomega.2c07271

[53] K. Fukui, T. Yonezawa, H. Shingu, A molecular orbital theory of reactivity in aromatic hydrocarbons, J. Chem. Phys. 20 (1952) 722-725. https://doi.org/10.1063/1.1700523

[54] R.G. Pearson, Absolute electronegativity and hardness correlated with molecular orbital theory, Proc. Natl. Acad. Sci. 83 (1986) 8440-8441. https://doi.org/10.1073/pnas.83.22.8440

[55] R.G. Parr, R.G. Pearson, Absolute Hardness: Companion Parameter to Absolute Electronegativity, J. Am. Chem. Soc. 105 (1983) 7512-7516. https://doi.org/10.1021/ja00364a005

[56] A. Niazi, S. Jameh-Bozorghi, D. Nori-Shargh, Prediction of toxicity of nitrobenzenes using ab initio and least squares support vector machines, J. Hazard. Mater. 151 (2008) 603-609. https://doi.org/10.1016/j.jhazmat.2007.06.030

[57] V. Hadigheh Rezvan, Molecular structure, HOMO-LUMO, and NLO studies of some quinoxaline 1,4-dioxide derivatives: Computational (HF and DFT) analysis, Results Chem. 7 (2024) 0-7. https://doi.org/10.1016/j.rechem.2024.101437

[58] Y. T. Lee, T. Ozaki, OpenMX viewer: A web-based crystalline and molecular graphical user interface program, J. Mol. Graph. Model. 89 (2019) 92-98. https://doi.org/10.1016/j.jmgm.2019.03.013

[59] M. Gajdoš, K. Hummer, G. Kresse, J. Furthmüller, F. Bechstedt, Linear optical properties in the projector-augmented wave methodology, Phys. Rev. B - Condens. Matter Mater. Phys. 73 (2006) 1-9. https://doi.org/10.1103/PhysRevB.73.045112

[60] S.Z. Karazhanov, P. Ravindran, A. Kjekshus, H. Fjellvåg, B.G. Svensson, Electronic structure and optical properties of ZnX (X=O, S, Se, Te): A density functional study, Phys. Rev. B - Condens. Matter Mater. Phys. 75 (2007) 1-14. https://doi.org/10.1103/PhysRevB.75.155104

[61] C.W. Chu, F. Chen, J. Shulman, S. Tsui, Y.Y. Xue, W. Wen, P. Sheng, A negative dielectric constant in nano-particle materials under an electric field at very low frequencies, Proc. SPIE, Strongly Correl. Electron Mater. Phys. Nanoeng. 5932 (2005) 59320X.

[62] H. Yan, C. Zhao, K. Wang, L. Deng, M. Ma, G. Xu, Negative dielectric constant manifested by static electricity, Appl. Phys. Lett. 102 (2013). https://doi.org/10.1063/1.4792064

[63] P. Ravindran, A. Delin, B. Johansson, O. Eriksson, J.M. Wills, Electronic structure, chemical bonding, and optical properties of ferroelectric and antiferroelectric, Phys. Rev. B - Condens. Matter Mater. Phys. 59 (1999) 1776-1785. https://doi.org/10.1103/PhysRevB.59.1776

[64] P. Singh, G. Dosovitskiy, Y. Bekenstein, Bright Innovations: Review of Next-Generation Advances in Scintillator Engineering, ACS Nano. 18 (2024) 14029-14049. https://doi.org/10.1021/acsnano.3c12381

[65] F. Moradi, D.A. Bradley, Z.H. Tarif, A. Khodaei, A. Basaif, S.A. Ibrahim, H.A. Abdul-Rashid, Time-resolved optical fiber measurements: a review of scintillator materials and applications, Radiat. Detect. Technol. Methods. 9 (2025) 1-16. https://doi.org/10.1007/s41605-024-00510-8

[66] H. Wei, J. Huang, Halide lead perovskites for ionizing radiation detection, Nat. Commun. 10 (2019) 1-12. https://doi.org/10.1038/s41467-018-07882-8

[67] N. Falsini, A. Ubaldini, F. Cicconi, A. Rizzo, A. Vinattieri, M. Bruzzi, Halide Perovskites Films for Ionizing Radiation Detection: An Overview of Novel Solid-State Devices, Sensors. 23 (2023) 1-25. https://doi.org/10.3390/s23104930

[68] W. Li, M. Li, Y. He, J. Song, K. Guo, W. Pan, H. Wei, Arising 2D Perovskites for Ionizing Radiation Detection, Adv. Mater. 36 (2024) 1-36. https://doi.org/10.1002/adma.202309588

[69] D.J. Robbins, On Predicting the Maximum Efficiency of Phosphor Systems Excited by Ionizing Radiation, J. Electrochem. Soc. 127 (1980) 2694-2702. https://doi.org/10.1149/1.2129574

[70] P. Dorenbos, P. Dorenbos, Light output and energy resolution of Light output and energy resolution of Ce 3 + -doped scintillators, 486 (2015) 208-213. https://doi.org/10.1016/S0168-9002(02)00704-0

[71] P.A. Rodnyi, P. Dorenbos, C.W.E. van Eijk, Energy Loss in Inorganic Scintillators, Phys. Status Solidi. 187 (1995) 15-29. https://doi.org/10.1002/pssb.2221870102

[72] P. Dorenbos, Fundamental limitations in the performance of Ce3+-, Pr 3+-, and Eu2+-activated scintillators, IEEE Trans. Nucl. Sci. 57 (2010) 1162-1167. https://doi.org/10.1109/TNS.2009.2031140

[73] C.A. Klein, Bandgap dependence and related features of radiation ionization energies in semiconductors, J. Appl. Phys. 39 (1968) 2029-2038. https://doi.org/10.1063/1.1656484

https://doi.org/10.66000/3110-9772.2025.01.05